Numerical Modeling of Antenna Arrays for Rapidly Deployable Radio Networks (RDRN) Part I: Far-Field Patterns of a Cylindrical Conformal Array of Axial Electric Dipoles

Deb Chatterjee,
Graduate Research Assistant

and,

Richard G. Plumb
Associate Professor

Radar Systems and Remote Sensing Laboratory (RSL) and
Telecommunication and Information Sciences Laboratory (TISL)
Department of Electrical Engineering and Computer Science
The University of Kansas Center for Research, Inc., (CRINC)
2291 Irving Hill Road, Lawrence, Kansas 66045-2969

March 1996

Abstract

Futuristic wireless communication systems must perform in environments that generate scattering from various obstacles which in turn cause multipath effects to be dominant. This results in degradation in the overall performance that can be avoided if the antennas have narrow beamwidths and low sidelobes. Advanced designs for Rapidly Deployable Radio Network (RDRN) systems are required to consider transmission at single frequency to several mobile users in a single frequency cell. This in turn requires narrow beam, low-sidelobe antenna patterns in order to obtain diversity between closely located users in a single cell. In this report analysis of an array of $\frac{\lambda}{2}$, axial, electric dipoles radiating in presence of a conducting cylinder is presented. The amplitude excitations are determined by Hamming and Taylor distributions while the phase excitations are determined by using an even symmetric quadratic phase taper. Once the complex excitations were found the far-field patterns were computed via the Numerical Electromagnetics Code - Basic Scattering Code (NEC-BSC). The mutual coupling has not been considered in this report. The results show that an interelement spacing between 0.4λ and 0.6λ may be chosen in order to avoid appearence of higher peaks close to the boresight mainbeam. This criterion has also been used to propose an algorithm to design the array geometry and the complex excitations. It was found that even symmetric phase taper provided superior pattern topography in addition to the amplitude taper. Indepenent control of the amplitude and phase excitations indicate that the Digital BeamForming (DBF) technique can be used to design high-performance cylindrical arrays.

Contents

List of Figures

Chapter 1

Introduction

Wireless communication systems operate in a rapidly changing environment and hence must continuously adapt to changes in channel topology. Furthermore, it is also desired that reception errors due to multipath effects be minimal. This requires design of narrow beamwidth, low-sidelobe antennas [1],[2] which increases security in both transmission and reception. Furthermore for a wider range of communication under emergency situations, such systems must have a 360^0 coverage in the azimuth plane [2]. Consequently it is important to study conformal or multiface planar arrays which can additionally generate multiple beams [3] and also have low multipath effects. The subject of this report is to study an array of axial, $\frac{\lambda}{2}$ electric dipoles in presence of a conducting circular cylinder for applications to wireless systems.

Adaptive array antennas have been studied earlier [4]-[6]. Adaptivity of antennas is realized by placing nulls in the direction of any jamming or interfering signal [6]. This amounts to change in overall pattern. Successful performance of a wireless system depends on the agility of the antenna to adapt to the environment or link topology. It has been shown that independent control of amplitude and phase excitation [7]-[9] can help realizing antenna designs which have higher degrees of freedom in the signal, allowing generation of multiple beams [10] carrying variety

of information. One can conclude from [7] that independent control of complex excitation can provide better pattern topography. The purpose of this investigation is to analyze arrays which have narrow beamwidths and lower sidelobes. This feature is studied by examining the effects of amplitude and phase tapers across the array elements. The results of this analysis can be used in designing advanced antenna systems for futuristic Rapidly Deployable Radio Networks (RDRN) [5].

Conformal arrays are generally difficult to analyze. The reason is that the Green's function for non-planar structures converge very slowly [11]-[13]. However, it is still possible to obtain near-field information of a non-planar array by using very special forms of the appropriate Green's function [11]. The formulation of such special Green's functions require substantial development time. Consequently for preliminary analysis, the computation of mutual coupling is generally avoided. In this report the far-field patterns of the cylindrical array are obtained without mutual coupling. Therefore, bandwidth information for a wireless system cannot be obtained from the preliminary results presented in this report.

One can analyze the effects of the adaptivity by formulating the array problem using optimization techniques[6],[14]-[17]. As shown in [14], far-field pattern of arrays is intimately connected to the improved performance of adaptive arrays. Thus an array with low sidelobes and narrow beamwidths is a good candidate for an adaptive array than the one with higher sidelobes and broader beamwidths. However for advanced antenna architectures, one needs to include the effects of the antenna geometry for a full-wave analysis. Conformal microstrip antennas are a class of architectures that are lightweight and hence are rapidly deployable. However, the determination of the Green's functions of these antennas are very complicated and hence the algorithms in [14]-[17] are difficult to use for a complete full-wave analysis of these arrays. It is therefore prudent to select models that are close to the desired architecture of conformal arrays, yet simple to analyze. Hence the available formulations for conformal arrays [18]-[20] have not

been implemented here, due to their complexity. Instead the model studied here is identical to the one in [21],[22] since it is numerically easier to examine the characteristics of such arrays. This model is a single-ring array of $\frac{\lambda}{2}$, axial, electric dipoles in presence of a conducting circular cylinder.

In chapter 2 the general characteristics of wireless antennas have been presented from [1] in section 2.1. The technique by which the amplitude and phase excitations of elements in a circular array are determined is shown in section 2.2. This technique is simpler and simulates the Digital BeamForming (DBF) technique [7]. In this technique the amplitude excitations are determined from [13] and the phases are found following the analysis in [23]. Once the complex (amplitude and phase) excitations are known, the patterns can be found from the exact or approximate formulas in [24],[25]. These approximate formulas have been shown to work in a variety of practical modeling situations and are also simple to use [26]-[28]. To that end, the NEC-BSC code [29] can be used which contains these approximate formulas. The NEC-BSC code requires antennas to be off the cylinder curved surface by a quarter wavelength. To that end, additional validation results can be found in [30].

For futuristic wireless antennas, conformal microstrip antennas are potential candidates [1],[2]. Bandwidth enhancement of microstrip antennas require rigorous modeling of the feed geometry. However it appears from the recent investigations in [31] that similar work needs to be extended to non-planar substrate configurations.

In chapter 3 results from the NEC-BSC code are presented followed by an algorithm which can determine the array geometry from a given set of specifications. These results have also been included in [32],[33].

In chapter 4 the status of current and future investigations have been included, followed by summary and conclusions in chapter 5.

3

Chapter 2

Characteristics of RDRN Switch Antennas

2.1 Introduction

In this chapter the desired characteristics of antennas for wireless communication applications are discussed. It is important for wireless antennas to be able to adapt to the changing environment (link). This suggests that some degree of adaptivity is mandatory for wireless antennas [1]. The adaptive nature of a wireless antenna manifests itself in changing the overall far-field pattern. This is realized by changing the complex excitations of each element in the array. Determination of these complex weights for a specified pattern topography is the fundamental problem for antennas with applications to wireless communications. In section 2.2 the desirable features of a wireless communication antenna are illustrated. The problem of determining the complex excitations is outlined in this section. In addition, the technique of Digital Beamforming (DBF) [7], is examined in view of its potential applications to wireless communications. In section 2.3 the method by which the DBF technique can be simulated, is presented.

2.2 General Problems Associated with the RDRN Antenna Performance

The desirable features of any wireless communication system are shown in Fig. 2-1. A good design would entail an in-depth analysis of all the antenna features that are shown here [1]. It is clear from Fig. 2-1, that a high-performance wireless antenna would have a reasonably high Signal-to-Interference-plus-Noise Ratio (SINR). This means that the antenna should be able to reject interfering signals coming in from arbitrary directions [1],[2],[4],[6]. This implies that arbitrary beamwidths, low sidelobes, and nulls in the direction of jamming signals should be realizable in order to maintain a good pattern shape. Such features should be available for the complete 360^0 scan range of the antenna.

A base-station antenna for wireless applications might have to support multiple users, frequency resuse and may also need to have sufficient diversity. This requires generation of multiple beams in addition to narrow beamwidths and low sidelobes. As discussed in [1, pp. 128-131], low sidelobe antennas increase the carrier-to-interference ratio (CIR) of a base station system. For RDRN systems, there may exist several users within a single frequency cell. It is desired to have simultaneous transmission at a single carrier frequency between two or more users with different modulation schemes. This implies that two or more antenna patterns should be generated which will have low sidelobes and narrow beamwidths. Such a feature will allow using the same frequency for closely spaced mobile users in the same cell. This is defined as "frequency reuse" for RDRN systems [5]. Other issues related to multiple beamforming for RDRN systems are discussed in [5]. Furthermore, as shown in [14], improvement adaptive performance is obtained for conventional antenna patterns having narrow beamwidths and lower sidelobes. Thus in analyzing the main features of RDRN base-station antennas, it is essential to develop techniques which will result in better pattern shape. The state-of-art

VLSI manafacturing technology allows integration of the antenna and r.f. hardware as one single module. This makes the complete system very lightweight and hence suitable for rapidly deployment. To that end, for a 360^0 azimuth coverage, the cylindrical array of rectangular microstrip patches appears suitable. A conceptual view of such an antenna is shown in Fig. 2-2.

Increased mutual coupling tends to degrade the bandwidth of antennas [1]-[3]. Unfortunately, mutual coupling analysis is computationally too intensive and shall be addressed separately in future investigations. Other issues depicted in Fig. 2-1, are not investigated here, and will be reported in later investigations.

A digital beamforming technique (DBF) for both transmission and reception is proposed. As discussed in [7], this technique allows increased degrees of freedom for the signal and hence one can generate multiple beams with several difefrent class of information. A proposed block diagram is shown in Fig. 2-3. The main feature of a DBF is to control the complex excitation $w_n = M_n e^{J\alpha_n}$. The amplitiude and phase controls can be achieved independently in a DBF technique. To simulate the DBF technique, it is necessary to examine the effects of both amplitude and phase tapers on the far-field patterns of a cylindrical array. This technique is described below.

2.3 Analysis of the Cylindrical Array For RDRN Applications

Satisfactory performance of a wireless communication antenna depends on its ability to continuously adjust to the environment or link. The link characteristics changes rapidly and can cause interfering signals to be incident along the direction of the mainbeam of the antenna. The antenna must sense the direction of this interfering signal (or noise) and place nulls in its pattern along the direction of this jamming signal. The placing of these nulls along the direction of the jamming sig-
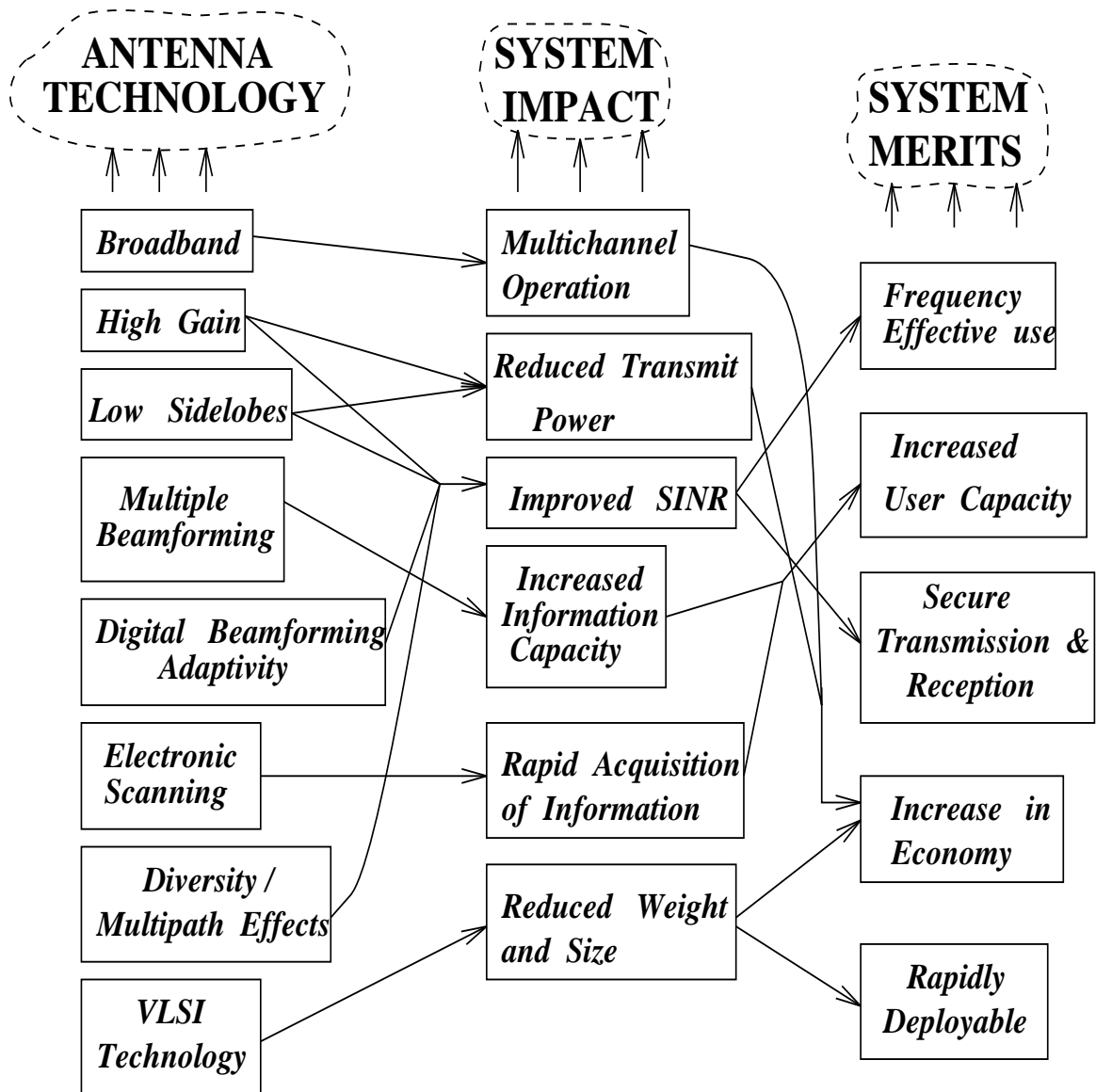
Figure 2-1: Impact of antenna parameters on the performance of a wireless communication system.

(a)

$\varepsilon = \varepsilon_r - j\,\varepsilon_i$

conducting ground plane

a single, metallic, rectangular patch element.

(b)
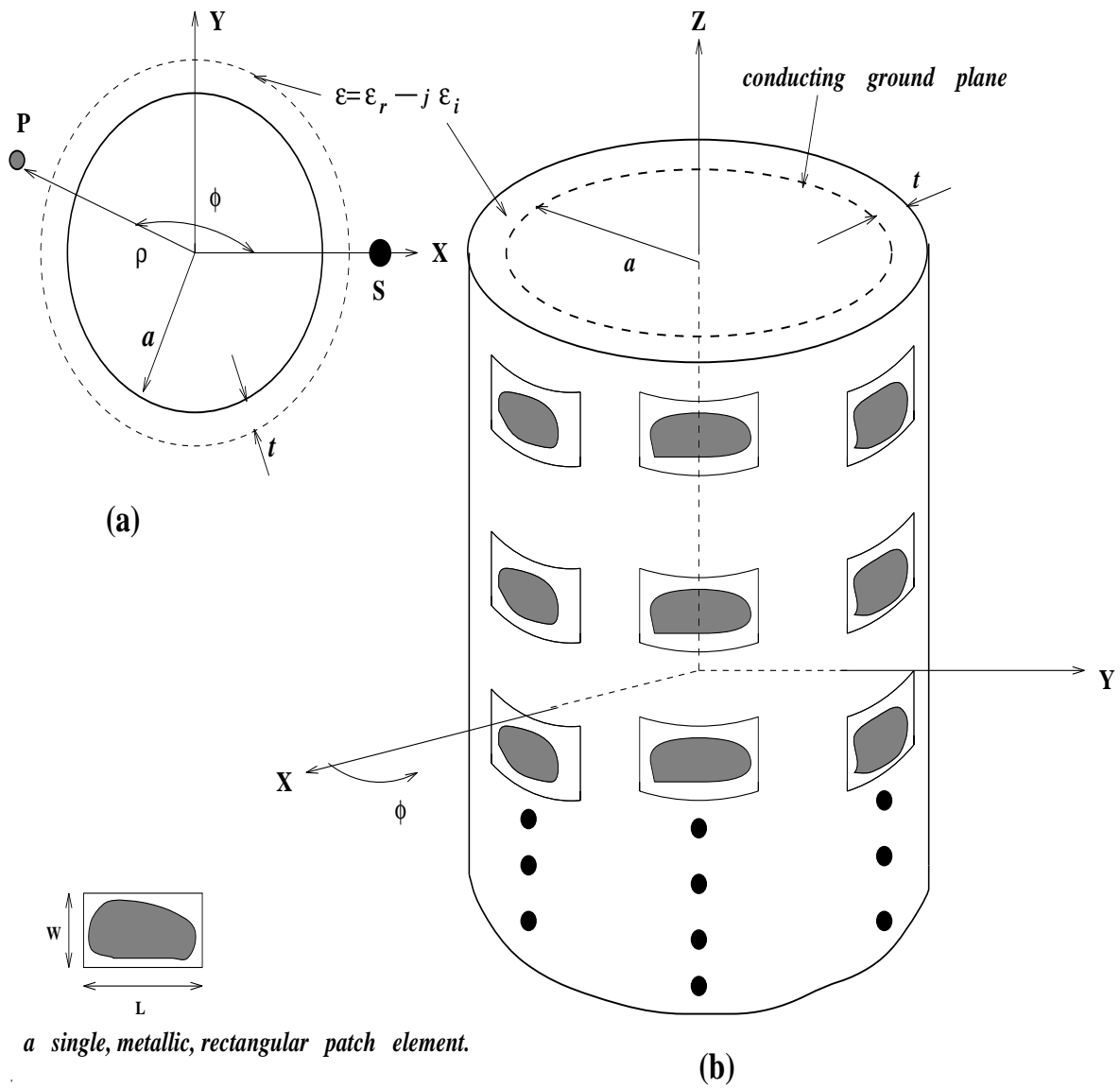
Figure 2-2: The general architecture of a cylindrical array of rectangular microstrip patches.

(a) Transmit Mode
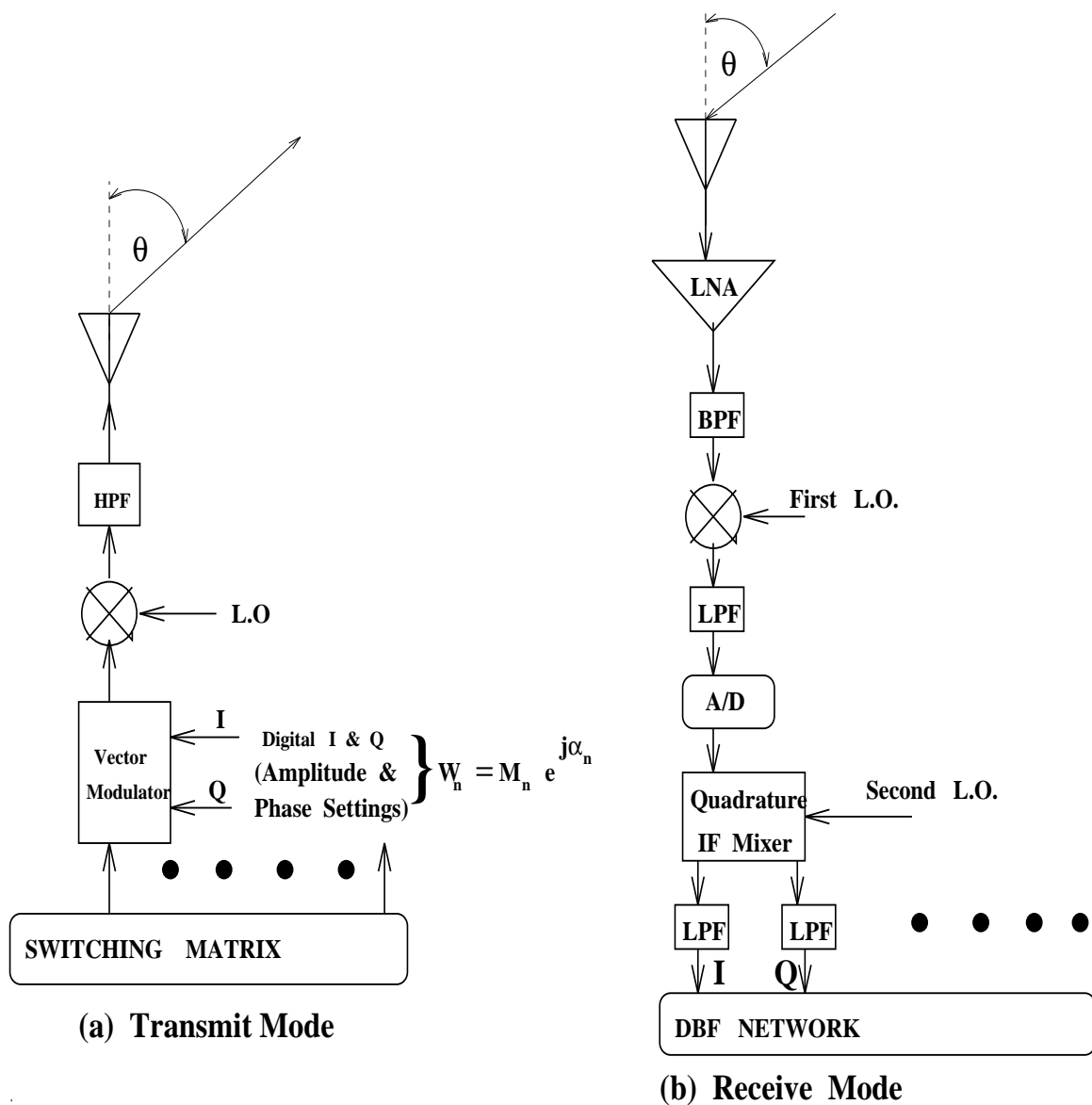
(b) Receive Mode

Figure 2-3: Suggested block diagrams of digital beamforming antenna systems in both transmit and receive modes of operation. The beamforming is achieved by controling the complex excitation w_n of each element in the array.

nal requires control of the complex excitation amplitudes of the array. These class of problems have been studied extensively in [6],[14],[15]. The general problem is to determine these complex weights given the direction of the jamming signal, overall pattern. Other constraints maybe placed in addition to the ones described earlier. The numerical algorithms required to determine these complex weights are computationally intensive [6]. In [14] it has been shown that the SINR of an adaptive array is mathematically related to the the conventional (non-adaptive) array pattern. Increase in inter-element mutual coupling has been shown to degrade the transient response of an adaptive array [15]. If the transient response is slower, then the overall system performance degrades because the antenna takes a longer time to adjust to the complex excitation weights. Consequently it turns out logical to examine the far-field patterns and the interelement mutual coupling for the conventional (non-adaptive) array. In this report the far-field patterns without mutual coupling are addressed first. The effects of mutual coupling will be reported separately in future.

One of the important techniques of antenna synthesis, that is fast gaining importance, is the development of suitable optimization proceedures for minimizing the norm (or mean square distance) between the array factor and the desired radiation pattern [17]. In yet another proceedure [23] the complex excitation weights are determined by exercising more control on the overall sidelobe topology. Some of the results obtained in [23] are particularly interesting for our present analysis. These will be discussed later in this section.

Analysis of the array shown in Fig. 2-2 is quite involved because the available mathematical formulations [18]-[20] for conformal microstrip patches converge very slowly, requiring significant analytical pre-processing before their numerical implementation. For cylindrical structures determination of the complex waves [18] become very complicated as compared to planar configurations [34]. This is because the nature of the transcendental equation to be solved is far more com-

plicated in the former case. Furthermore, one needs to examine the limitations of the formulations in [18]-[20] before they can be used for determining the array pattern. All these considerations suggested the choice of a simpler model for which the formulations are simpler to implement numerically. To that end, the model closest to Fig. 2-2 is an array of axial, electric, $\frac{\lambda}{2}$ dipoles in presence of a conducting cylinder, shown in Fig. 2-4. This model retains all the canonical features of the conformal array structure shown in Fig. 2-2.

It turned out after careful analysis of the problem that for relatively simpler configurations shown in Fig. 2-4 (a), the determination of complex weights become substantially complicated because the overall cylindrical array factor is non-separable in orthogonal planes [3, ch. 4],[11]. Thus unlike the case of planar arrays one cannot directly use principles of linear array synthesis in case of cylindrical arrays. This mathematical difficulty can be avoided if some degree of flexibility based on physical reasoning is employed, as discussed below.

If there are N_{elm} equally spaced dipoles disposed over an angular sector φ_s, then these locations can be projected onto a linear array as shown in Fig. 2-4 (b). Assuming that the element pattern is a cosine variation in the azimuth ($\theta = 90^0$) plane, one can use the principles of linear array theory [13, ch. 10] to determine the amplitude weights. Note that the elements are unequally spaced over the linear array.

The amplitudes of the currents at the locations can then be computed via Hamming [12, p. 232]

$$i(y_m) = 0.08 + 0.94 \cos^2(\frac{\pi y_m}{L})$$ (2.1)

and the Taylor [13, p. 547, (10-86)]

$$i(y_m) = \frac{\lambda}{L}\left[1 + 2\sum_{n=1}^{\overline{n}-1} f(n, A, \overline{n}) \cos(\frac{2\pi n y_m}{L})\right]$$ (2.2)

11

(a)

(b)

↑ **Single Dipole Element**

● **element locations**

φ_s **angular span of the sector**

L **projected length of the sector**
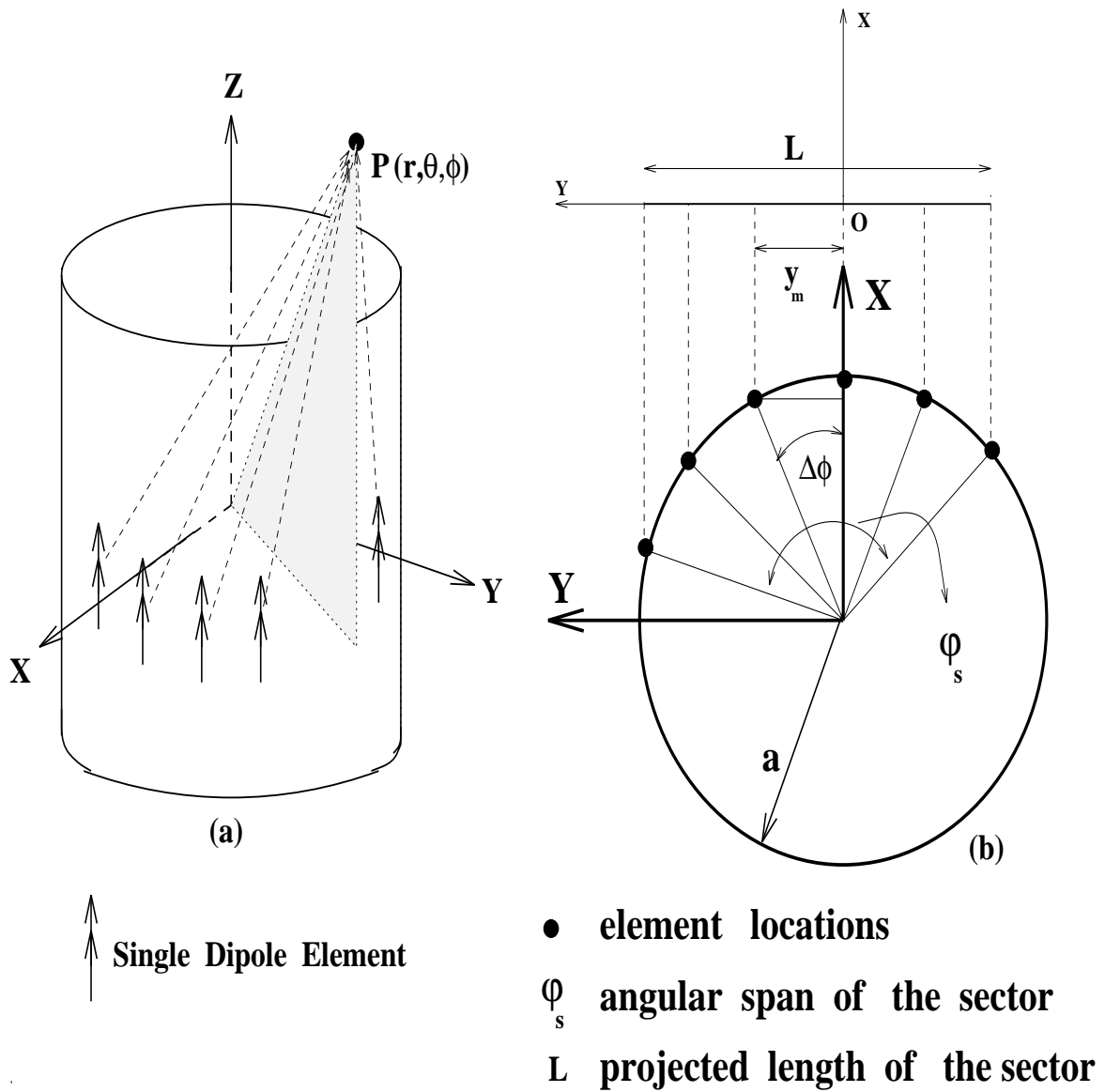
Figure 2-4: Geometry of a Conformal Cylindrical Array for Modeling RDRN Switch Antennas

distributions, respectively. In (2.2) $\overline{n}$ is the number of 'equal-height' sidelobes contiguous to the mainbeam [13]. The peak levels of the sidelobes exhibit a $\frac{\sin x}{x}$ envelope decay beyond $\overline{n}$ [3],[13]. The quantities y_m and L in are shown in Fig. 2-4 (b). The 'design' (or 'equal-height') sidelobe level for the Taylor line source determines A and $f(n, A, \overline{n})$ in (2.2) [13, p. 547]. These are omitted here for brevity. Thus knowing $\overline{n}$ and the sidelobe level, one can determine the currents via Eqs. (2.1) and (2.2).

Once the amplitude of the currents are computed via (2.1) and (2.2), the fields radiated from each elements can be superposed in the far zone to determine the complete pattern [3],[13], ignoring mutual coupling effects. It turned out convenient to use the NEC-BSC code [29] that is ideally suited for such calculations. However the NEC-BSC code does not allow the sources to be mounted on a cylinder due to limitations in its formulations [25],[26]. It turned out from the analysis in [21],[22] that dipoles should be placed no less than $\frac{\lambda}{4}$ off the cylinder surface for engineering approximations. This has also been verified by comparing the NEC-BSC and eigenfunction results and are presented in Appendix A.

When the source is off the cylinder by a distance h as in Fig. 2-5, the projected length

$$L = 2(a + h)\sin\left[\frac{N_{elm}\phi_{inc}}{2}\right], \tag{2.3}$$

where N_{elm} are the total number of elements in the angular sector φ_s. The distance

$$y_m = (a + h)\sin[(m - 1)\Delta\phi], \tag{2.4}$$

where $m = 1, 2, 3, ..., N_{elm}$. The angular increment ϕ_{inc} in Fig. 2-4 is given by

$$\phi_{inc} = \frac{\varphi_s}{N_{elm} - 1}. \tag{2.5}$$

The interelement spacing along the arc length is $s = (a + h) \times \phi_{inc}$. The amplitude

PERFECTLY CONDUCTING CYLINDER

AXIAL ELECTRIC DIPOLES

φ_s

a

Y ARC-LENGTH

$s=(a+h)\times \phi_{inc}$

h

ϕ_{inc}

BORESIGHT AXES

$\dfrac{\varphi_s}{2}$

X
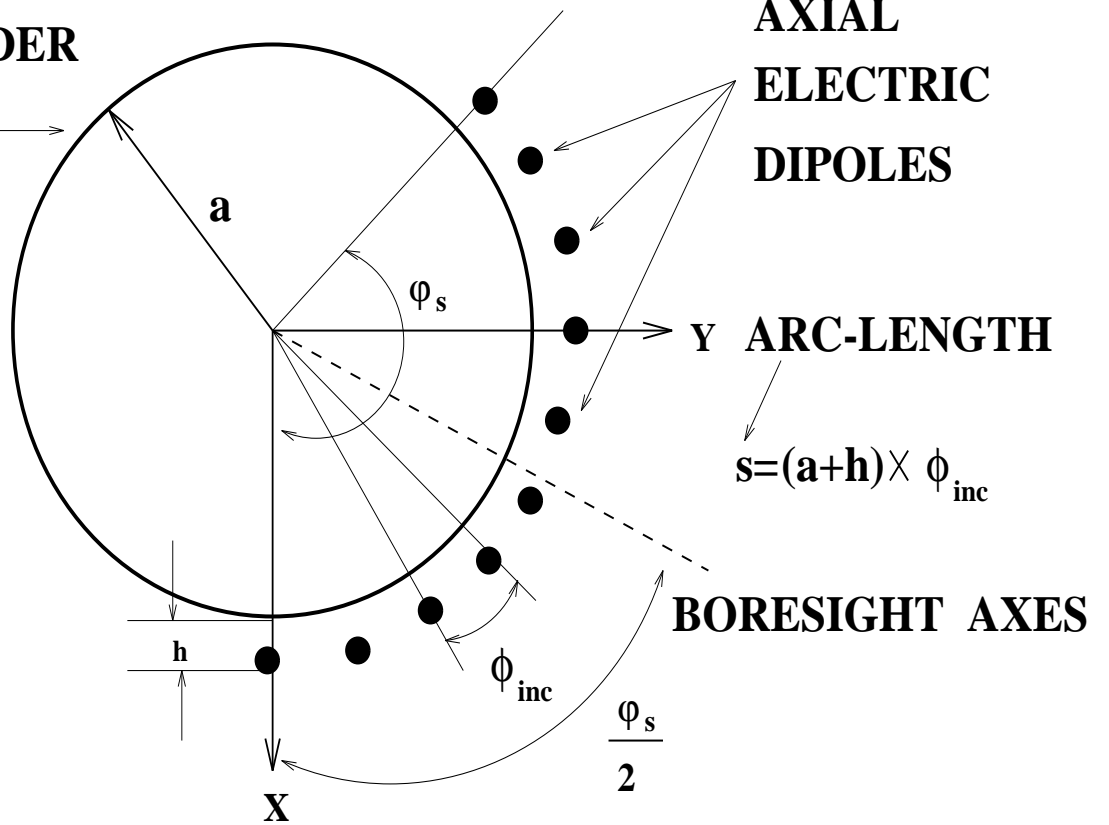
Figure 2-5: Additional details for the geometry in Fig. 2-4. Note that in Fig. 2-4 $\Delta\phi \equiv \phi_{inc}$, where ϕ_{inc} is shown here.

excitations can be determined via (2.1) and (2.2). The sources are defined in the NEC-BSC code by the amplitude and phase of excitations.

In traditional antenna synthesis problems the amplitude taper is determined from a given set of far-field specifications [13]. In general, the information about the element phase excitation is used in beam scanning applications [12]. However, even in such cases the design of elements is based upon amplitude excitation only. In DBF systems information regarding phase excitation is explicitly used to control the pattern shape. As shown in Fig. 2-3, this phase control is achieved independently of the amplitude excitation across the elements. This suggests that to simulate DBF systems the effects of phase taper needs to be studied independently in addition to the amplitude taper.

From the results in [23, Fig. 2], it appeared that a parabolic (or quadratic) phase taper could provide improved pattern control. This further suggested examining of even symmetric phase tapers on the overall array pattern. To that end, parabolic, triangular and exponential phase tapers were chosen for simulation of the DBF technique. From [23, Fig. 2] the amplitude taper appeared similar to an even symmetric distribution. Thus (2.1) and (2.2) were used in determining the amplitude excitations of the elements.

To determine the excitation phases α_m across each of the N_{elm} elements in the array sector φ_s, a continuous, even, phase function needs to be sampled at the discrete element locations given by y_m in (2.4). This suggests that α_m be a function of y_m. To that end, the even symmetric phase tapers

$$\alpha_m = \begin{cases} 360 \times \left(\frac{y_m}{L}\right)^2, & \text{parabolic} \\ 360 \times \frac{y_m}{L}, & \text{triangular} \\ 180[1.0 - e^{-\left(\frac{\tau y_m}{L}\right)^2}] & \text{exponential} \end{cases} \qquad (2.6)$$

were found suitable for determining the phases across each elements. The projected length L is given by Eq. (2.3). In Eq. (2.6) α_m is in degrees and τ is the

control parameter which can be varied to obtain different phase tapers across the array.

Once the phase and amplitude taper can be found, they can be used as input data for defining the source configuration to NEC-BSC code. The NEC-BSC code can predict fields from antennas in presence of obstacles [26]. A summary of the theoretical formulations in NEC-BSC code can be found in [25]. In addition to the amplitude and phase excitations, the location of the phase-centers of the $\frac{\lambda}{2}$ dipoles need to be defined as input to the NEC-BSC code. This can be readily done from the geometry in Fig. 2-5. Note that the locus of these phase-centers form a concentric circle of radius $a + h$. The centers are located at intervals of $\Delta\phi \equiv \phi_{inc}$, which can be found via (2.5). Thus for the pth dipole location in the ring, one can determine the locations $x_p = (a + h)\cos[\phi_{inc}(p - 1)]$ and $y_p = (a + h)\sin[\phi_{inc}(p - 1)]$, from the geometry in Fig. 2-5. Since all dipole phase-centers are in the $\theta = 90^0$ (azimuth) plane, $z_p = 0$. In defining the source location, $h = \frac{\lambda}{4}$ is the minimum distance off the cylinder surface.

In employing the NEC-BSC code one has to define the source and pattern coordinate systems correctly. For the present problem, the axis of the cylinder can be chosen as the z axis of the pattern coordinate system. The pattern x and y axes can be defined exactly as in Figs. 2-4 and 2-5. The source coordinate for the pth dipole is such that the source z axis is parallel to the pattern (or cylinder) axis. The source x and y axes have to be defined so that the angular increment of $\Delta\phi$ is accounted for in defining these axes relative to pattern x and y axes.

The above information can be used to prepare the input datafile for the NEC-BSC code. The details are given in [29] and are omitted here.

Chapter 3

Numerical Results and Discussion

3.1 Introduction

In this chapter the far-field patterns of an array of axial electric dipoles in presence of a circular cylinder are analyzed. To examine the effectiveness of the proposed Digital BeamForming (DBF) technique, the effects of the amplitude and phase taper are studied in detail. The dependence of the antenna pattern on the interelement spacing is examined. The geometry under consideration is shown in Fig. 2-4. This geometry, as explained in chapter 2, can be analyzed using NEC-BSC code. The effects of pattern distortion near the boresight, due to creeping wave effects, are shown here. It is shown that by using suitable amplitude and phase tapers, this problem can be avoided. In these results mutual coupling is not considered. The mutual coupling can be incorporated by determining the currents on the individual elements of the array using the methods in [21]. This aspect will be reported in our future investigations. However the results presented here are still important since they illustrate the fundamental concepts of digital beamforming (DBF) antennas, in obtaining narrow beamwidths and low sidelobes.

It is a good computational practice to validate a general purpose computer code for a canonical problems. The NEC-BSC code can be verified against the exact eigenfunction formulation [24]. These validation results have been included in Appendix A. The formulations in the NEC-BSC code do not allow antennas to be mounted directly on the cylinder [25],[26],[29]. The source has to be located about $\frac{\lambda}{4}$ away from the curved surface. However it has been verified in [21],[22] that this does not alter significantly the far-field pattern if the cylinder radius $ka > 10$. Consequently it was decided to fix the distance $kh = \frac{\pi}{2} = 1.57$ in all the inputs to NEC-BSC code. The amplitude and phase tapers have been generated via the techniques developed in section 2.3. The individual results from NEC-BSC are discussed in section 3.2. In all the figures ka refers to the cylinder size and kh depicts the height above the cylinder surface as shown in Fig. 2-4. Furthermore the Taylor parameter $\bar{n}$ in Eq. (2.2) is designated by n in Figs. 3-7 to 3-16 for notational convenience. The total number of elements that are simultaneously excited is depicted as N_{elm} in these figures. The angular sector over which these N_{elm} elements are disposed is φ_s, and the inter-element arc-length is $\frac{s}{\lambda}$ as shown in Fig. 2-5. Most of the numerical data are shown in the respective figures themselves and hence are not repeated in the following section. Finally in section 3.3 and algorithm to determine the array geometry and the complex excitations is proposed.

3.2 Far-Field Patterns of a Conformal Array of Axial Electric Dipoles for RDRN Applications

The effect of the phase taper on far-field patterns is shown in Figs. 3-1 and 3-2. In Fig. 3-1 all the dipoles were identically represented by the excitation

18

$1.0 + j0.0 (1.0 \lfloor 0^0)$. In Fig. 3-2 the elements had an excitation defined by $1.0 e^{j\alpha_n}$ $(1.0 \lfloor \alpha_n^0)$. The individual element phases, α_n, were determined via Eq. (2.6). The azimuth angle Φ is measured positively from the x axis in Fig. 2-4 (a). The results show pattern degradation near boresight ($\Phi = 60^0$) for both cases. One can conclude, by comparing results in Figs. 3-1 and 3-2, that phase taper alone is not adequate for proper beam formation near boresight.

To investigate conditions under which a proper antenna beam is formed, effects of amplitude taper were investigated. The results are shown in Figs. 3-3 to 3-10. In these figures no phase taper was provided across the elements.

From Fig. 3-3 one can conclude that a Hamming amplitude taper can form a beam near borseight, unlike the patterns shown in Figs. 3-1 and 3-2. The result in Fig. 3-3 shows that the beamwidth for smaller cylinders tends to be larger. This is expected because the corresponding projected aperture length, L in Fig. 2-4 (b), is smaller.

In Figs. 3-4 and 3-5 the effect of interelement spacing, $\frac{s}{\lambda}$, on the patterns is examined. It may be recalled from Fig. 2-4(b) that $\frac{s}{\lambda}$ depends on the sector of excitation φ_s, cylinder radius ka and number of elements N_{elm} in the sector. One can generally conclude that for $\frac{s}{\lambda} \geq 0.5$ large peaks begin to appear, as shown in the two figures. (For $\frac{s}{\lambda} = 0.67$ in part (a) of Fig. 3-4, the appearence of these peaks may not be obvious; their presence maybe verified from the corresponding patterns in part (b).) These peaks appear when the interelement arc spacing is such that the corresponding linear spacing exceeds or is close to $\frac{\lambda}{2}$. As discussed in [12],[13] $\frac{\lambda}{2}$ spacings in linear arrays cause appearence of grating lobes. These results are for amplitude excitation only. Additional results, employing both phase and amplitude excitation will be discussed later in this section.

The results in Figs. 3-3 to 3-5 were generated using Hamming distribution as amplitude taper. To investigate the effects of amplitude taper in more detail, a comparison was performed between both Hamming and Taylor distributions, as
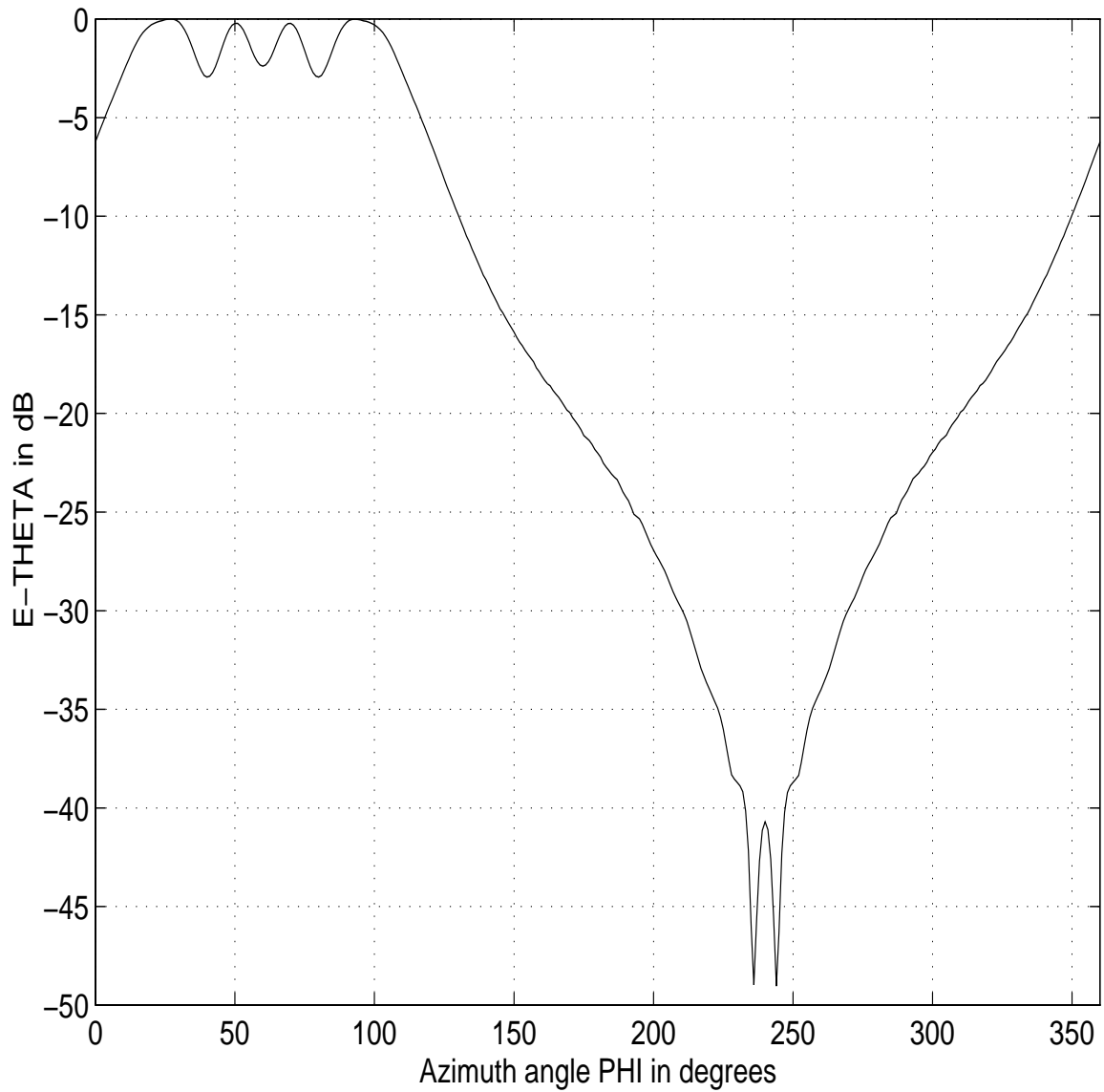
Figure 3-1: Far-field pattern for $ka = 20$ and $\frac{s}{\lambda} = 0.36$ in the $\theta = 90^0$ (azimuth) plane; $N_{elm} = 21$; $\varphi_s = 120^0$ and $kh = 1.57$. The pattern boresight (mainbeam maxima) is at $\Phi = 60^0$ and all elements are identically excited to $1\lfloor 0^0$.
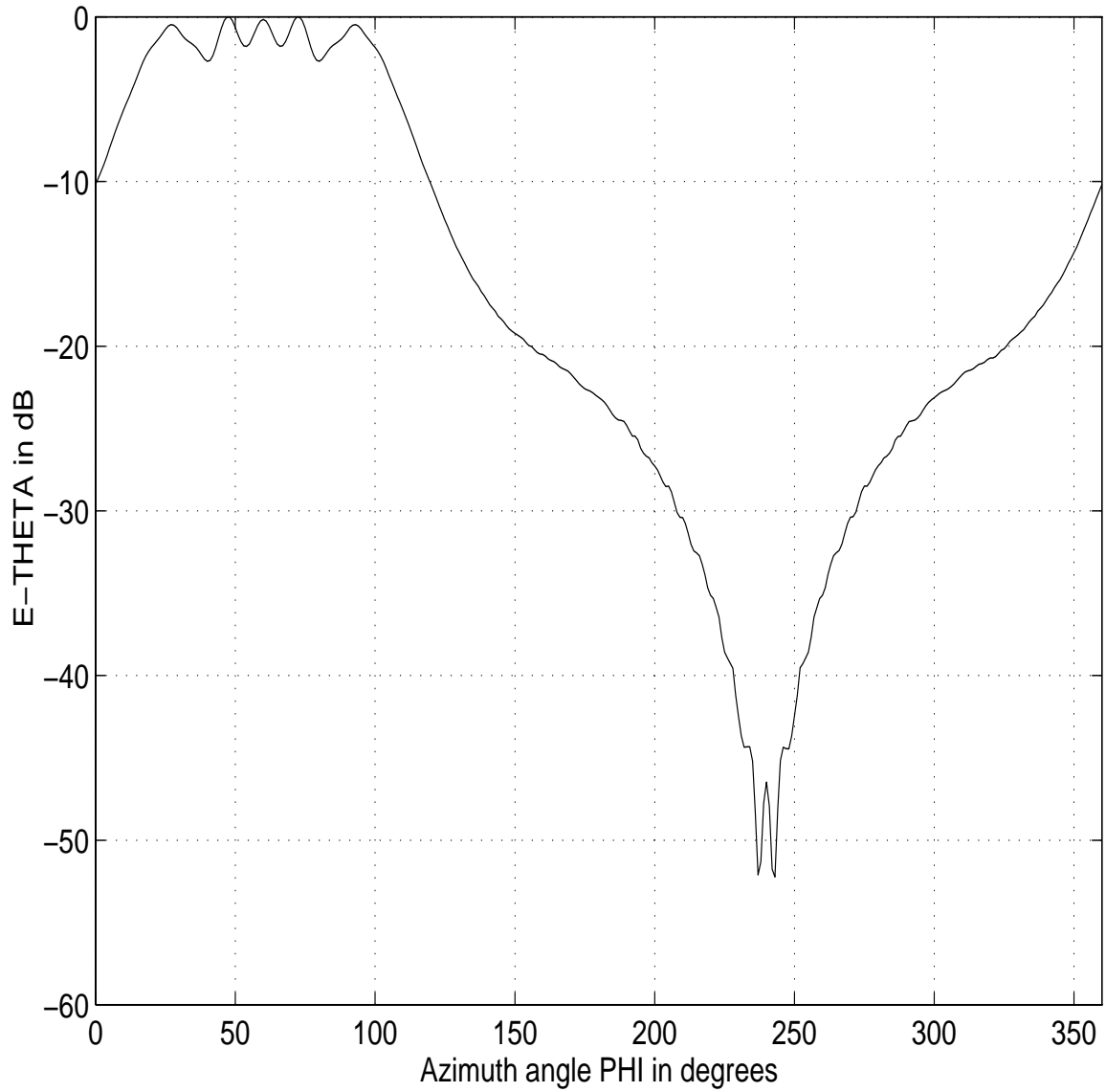
Figure 3-2: Far-field pattern for $ka = 31.4$ and $\frac{s}{\lambda} = 0.55$ in the $\theta = 90^0$ (azimuth) plane; $\mathrm{N}_{elm} = 21$; $\varphi_s = 120^0$ and $kh = 1.57$. The pattern boresight (mainbeam maxima) is at $\Phi = 60^0$ and the excitation for the mth element is $1\lfloor \alpha_m$, where α_m is given by Eq. (2.6).
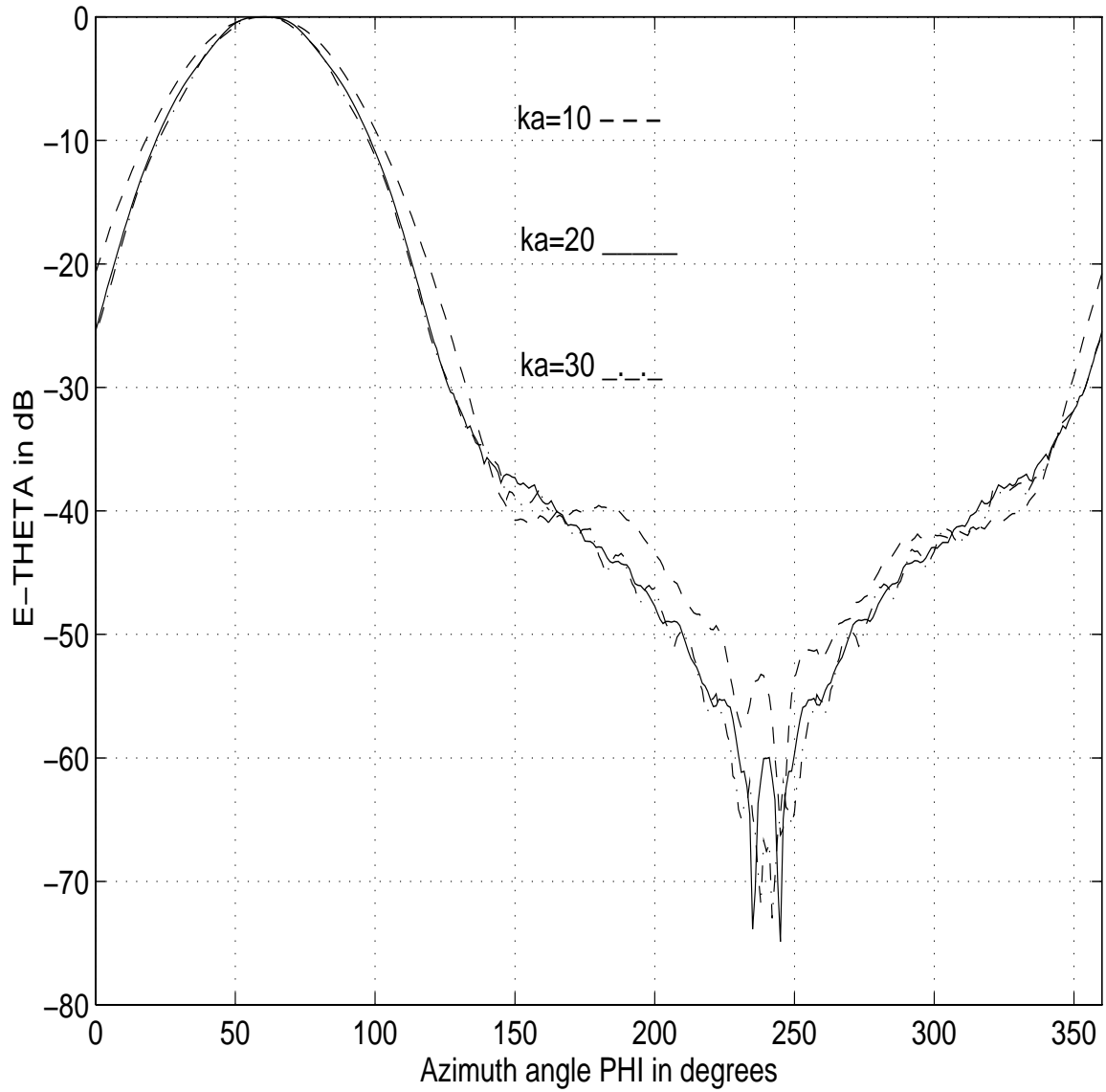
Figure 3-3: Far-field patterns for $ka = 10, 20, 30$ corresponding to $\frac{s}{\lambda} = 0.19, 0.36$ and 0.52, respectively in the $\theta = 90^0$ (azimuth) plane; $N_{elm} = 21$; $\varphi_s = 120^0$ and $kh = 1.57$. The boresight (mainbeam maxima) is at $\Phi = 60^0$. The amplitude taper was determined via Hamming distribution in Eq. (2.1).
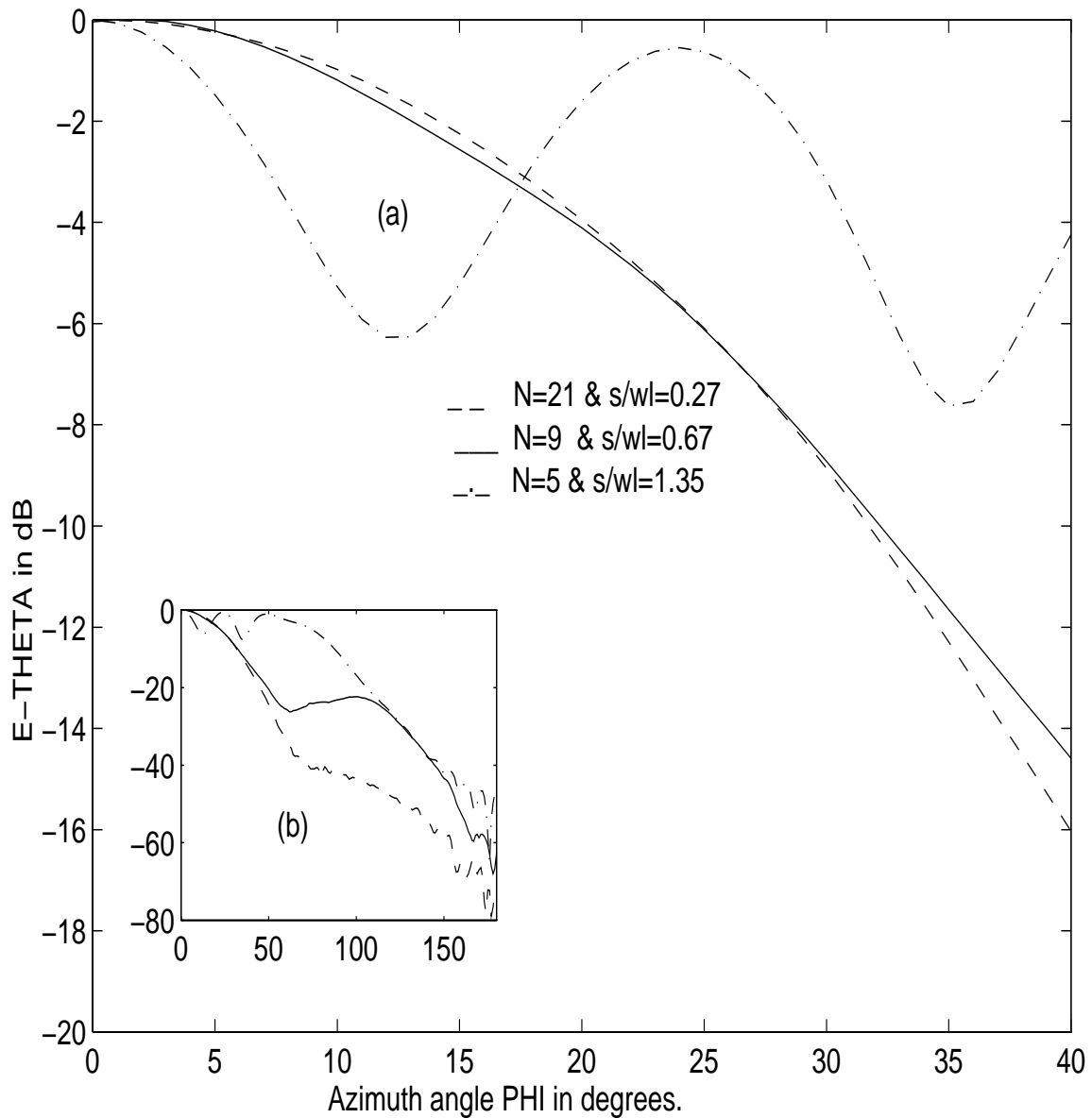
Figure 3-4: Comparison of $\theta = 90^0$ (azimuth) plane patterns for $ka = 20, kh = 1.57, f = 5\mathrm{GHz}$, and $\varphi_s = 90^0$ in Fig. 2-5. The amplitude taper was determined via Hamming distribution in Eq. (2.1). In this figure the boresight is at $\Phi = 0^0$.
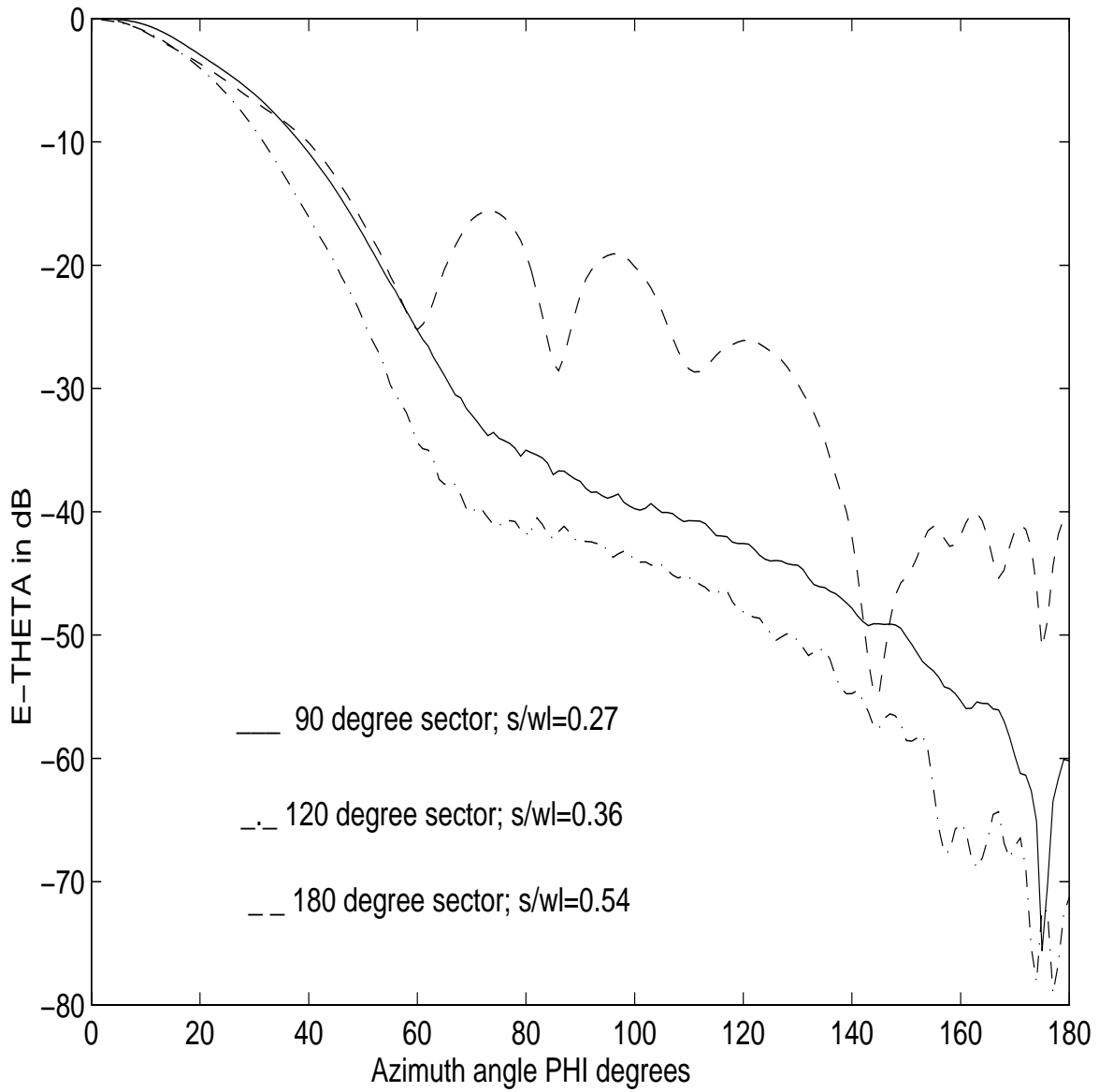
Figure 3-5: Comparison of $\theta = 90^0$ (azimuth) plane patterns for $ka = 20, kh = 1.57, f = 5\mathrm{GHz}$ and $N_{elm} = 21$. The amplitude taper was determined via Hamming distribution in Eq. (2.1). In this figure the boresight is at $\Phi = 0^0$.

defined via Eqs. (2.1) and (2.2), respectively. The results are shown in Figs. 3-6 to 3-10, which do not contain any phase taper.

The result in Fig. 3-6 show thye differences between Hamming and various Taylor distributions. The two distributions are very identical in overall shape.

In Figs. 3-7 to 3-8 the principal plane ($\theta = 90^0$) patterns are shown. The result in Fig. 3-7 shows that the Taylor parameter $\overline{n}$ does not produce any significant change in pattern. This is due to the fact the Taylor amplitude distributions for various $\overline{n}$ are almost the same for a design sidelobe of -40 dB, as shown if Fig. 3-6.

In Figs. 3-9 to 3-10 the E_θ component patterns in the elevation plane through the boresight are shown. (It maybe recalled that the boresight is at 60^0 for a 120^0 sector array.) In this plane the patterns are identical since no amplitude taper was applied in this plane. The single ring array, as shown in Fig.2-4(a), thus produces a fan-beam in the elevation ($\Phi = 60^0$) plane. This is expected because the array has a longer aperture length in the azimuth ($\theta = 90^0$) plane which produces a narrow beam in this plane.

One may generally conclude that an amplitude taper alone can form a beam along the boresight. In contrast, phase taper alone cannot form a beam near the same region.

The next set of investigations employed both amplitude and phase tapers. The amplitude taper for the results in these figures was generated via Taylor distribution, since it is widely used for pattern synthesis [12],[13]. The results are shown in Figs. 3-11 to 3-21. It is easy to conclude from these results that both amplitude and phase taper together can provide a superior pattern topography than using amplitude taper alone. This fact is supported by the results shown in Figs. 3-11 and 3-12. The solid line in Fig. 3-11 refers to the data shown in Fig. 3-3 for $ka = 20$. One can generally conclude that reduced sidelobes and narrower beamwidths can be obtained using the even-symmetric parabolic
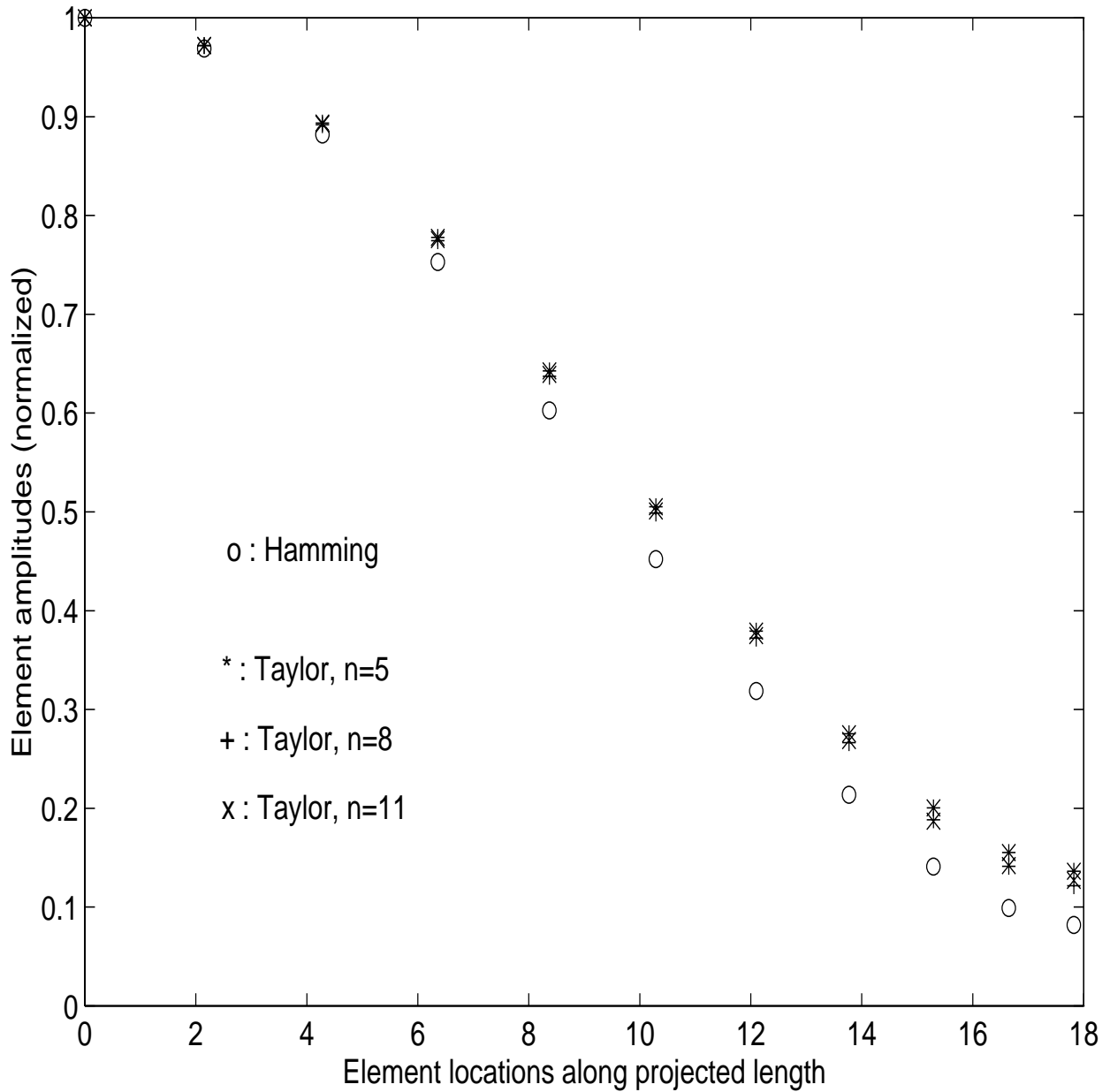
Figure 3-6: Amplitude distribution at discrete element locations in the projected linear array in Fig. 2-4 (b). Here $ka = 20, kh = 1.57$, $f = 5$ GHz, $\varphi_s = 120^0$ and $N_{elm} = 21$. Only one-half of the even-symmetric distributions in Eqs. (2.1) and (2.2) are shown. Here, $\bar{n}$ in Eq. (2.2) is designated by n and a design sidelobe level of -40 dB was used for Taylor distribution.
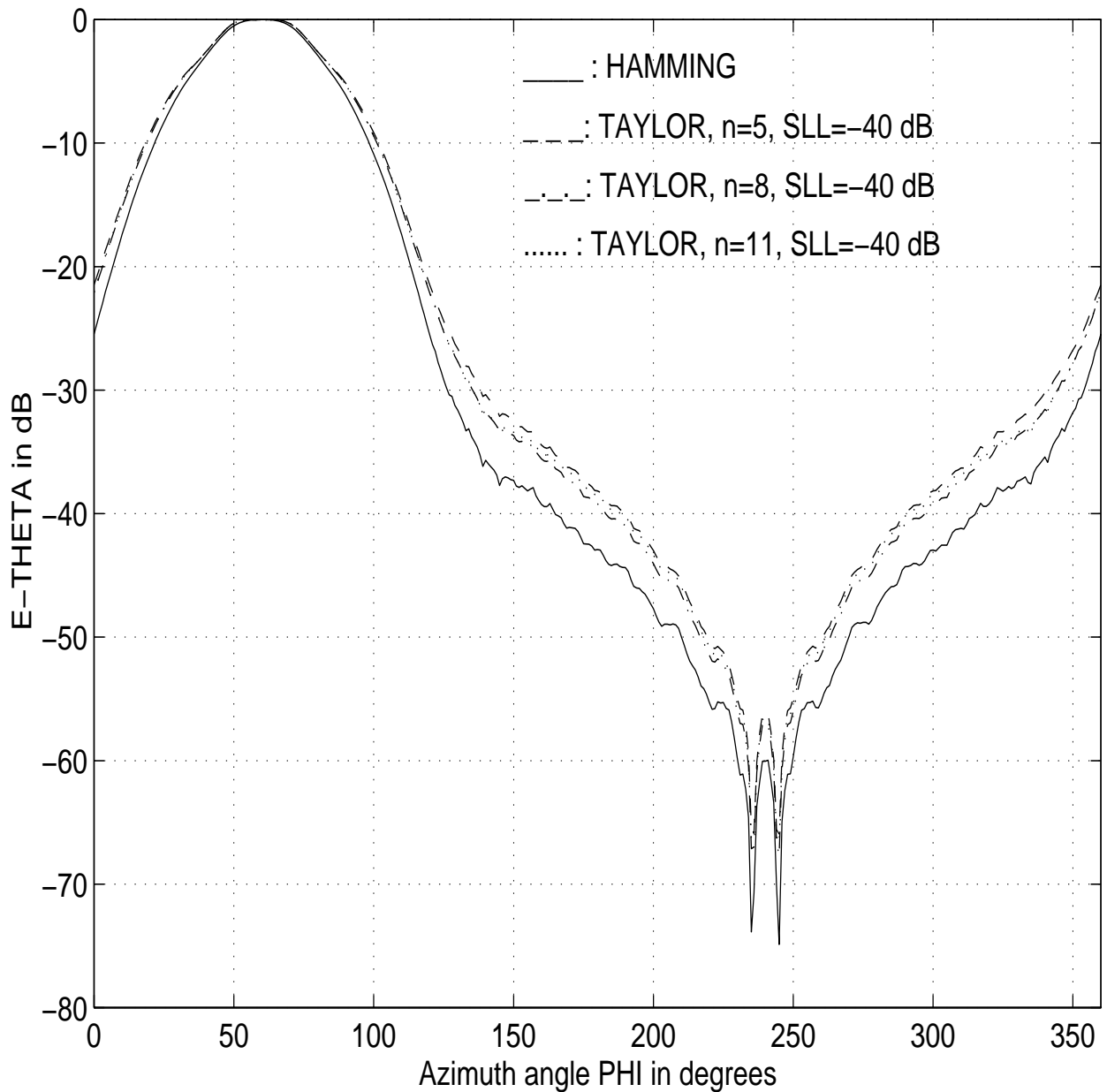
Figure 3-7: Far-field pattern comparisons between Hamming and Taylor distributions for $ka = 20$, $kh = 1.57$, $f = 5$ GHz, $\varphi_s = 120^0$, $N_{elm} = 21$ in the $\theta = 90^0$ (azimuth) plane. Here, $\overline{n}$ in Eq. (2.2) is designated by n and the pattern boresight (mainbeam maxima) is at $\Phi = 60^0$. The patterns are for the amplitude distributions in Fig. 3-6.
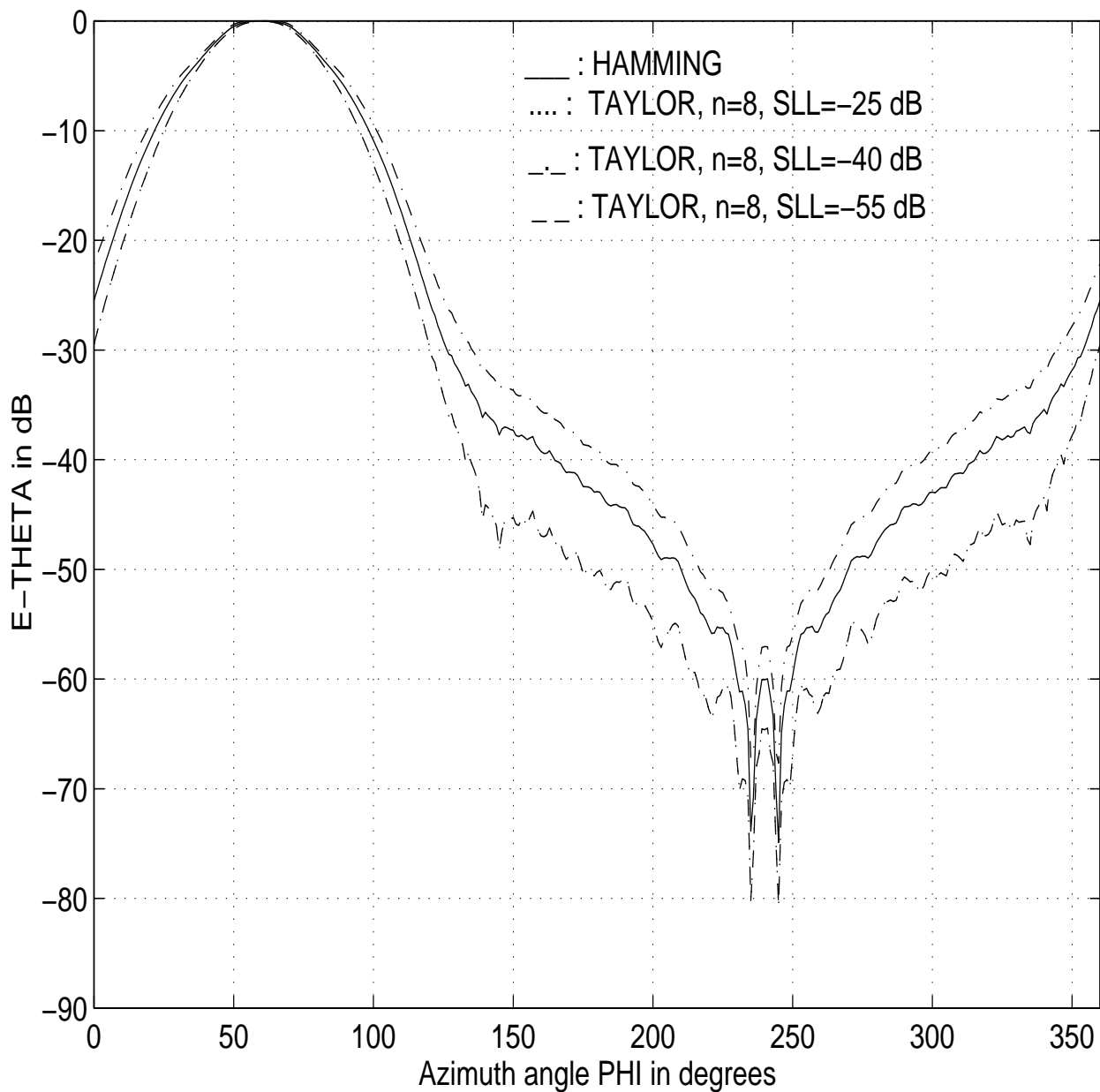
Figure 3-8: Far-field pattern comparisons between Hamming and Taylor distributions for $ka = 20$, $kh = 1.57$, $f = 5$ GHz, $\varphi_s = 120^0$, $N_{elm} = 21$ in the $\theta = 90^0$ (azimuth) plane. Here, $\overline{n}$ in Eq. (2.2) is designated by n and the pattern boresight (mainbeam maxima) is at $\Phi = 60^0$.
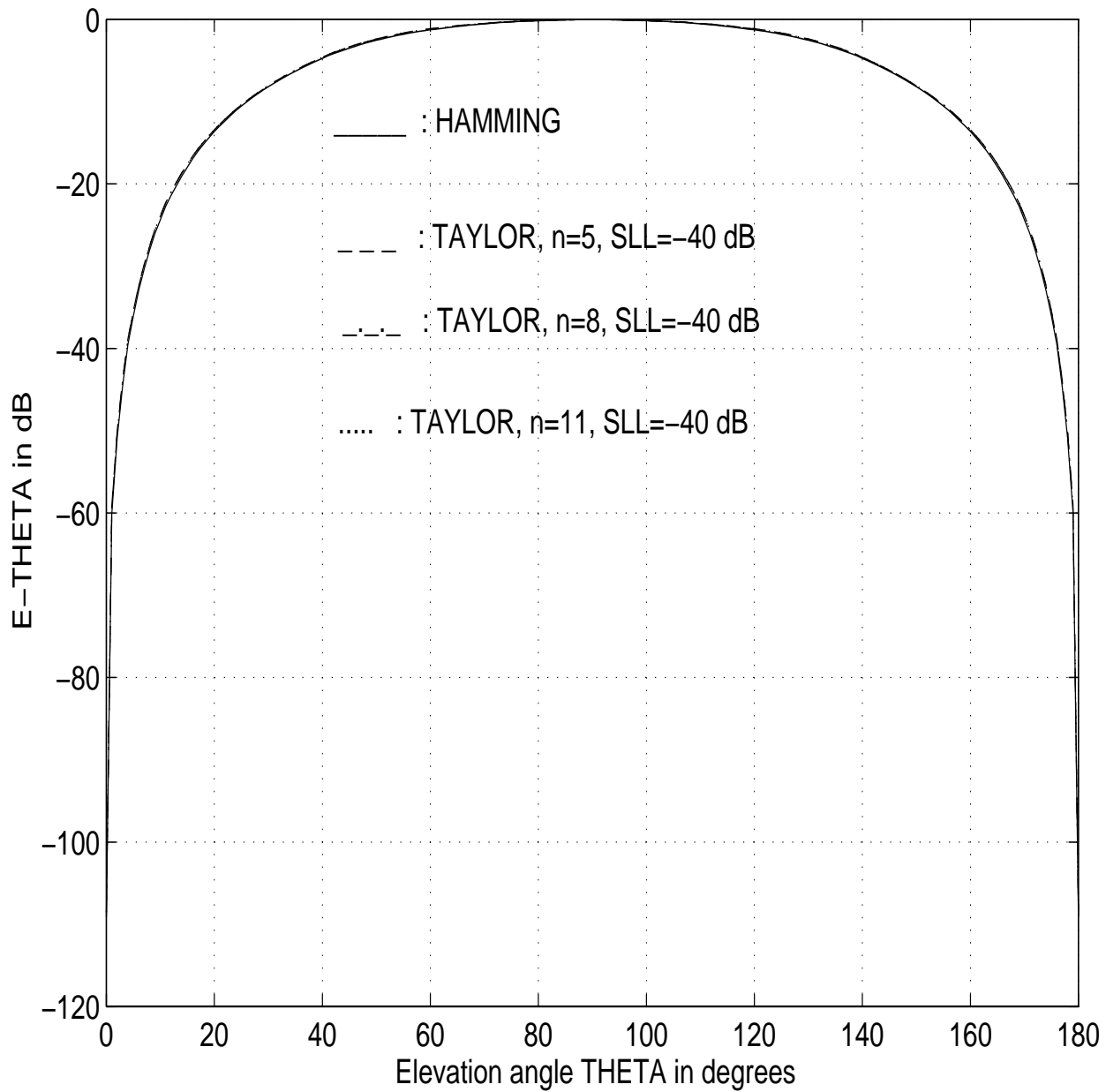
Figure 3-9: Far-field pattern comparisons between Hamming and Taylor distributions for $ka = 20$, $kh = 1.57$, $f = 5$ GHz, $\varphi_s = 120^0$, $N_{elm} = 21$ in the $\phi = 60^0$ plane. Here, $\overline{n}$ in Eq. (2.2) is designated by n.
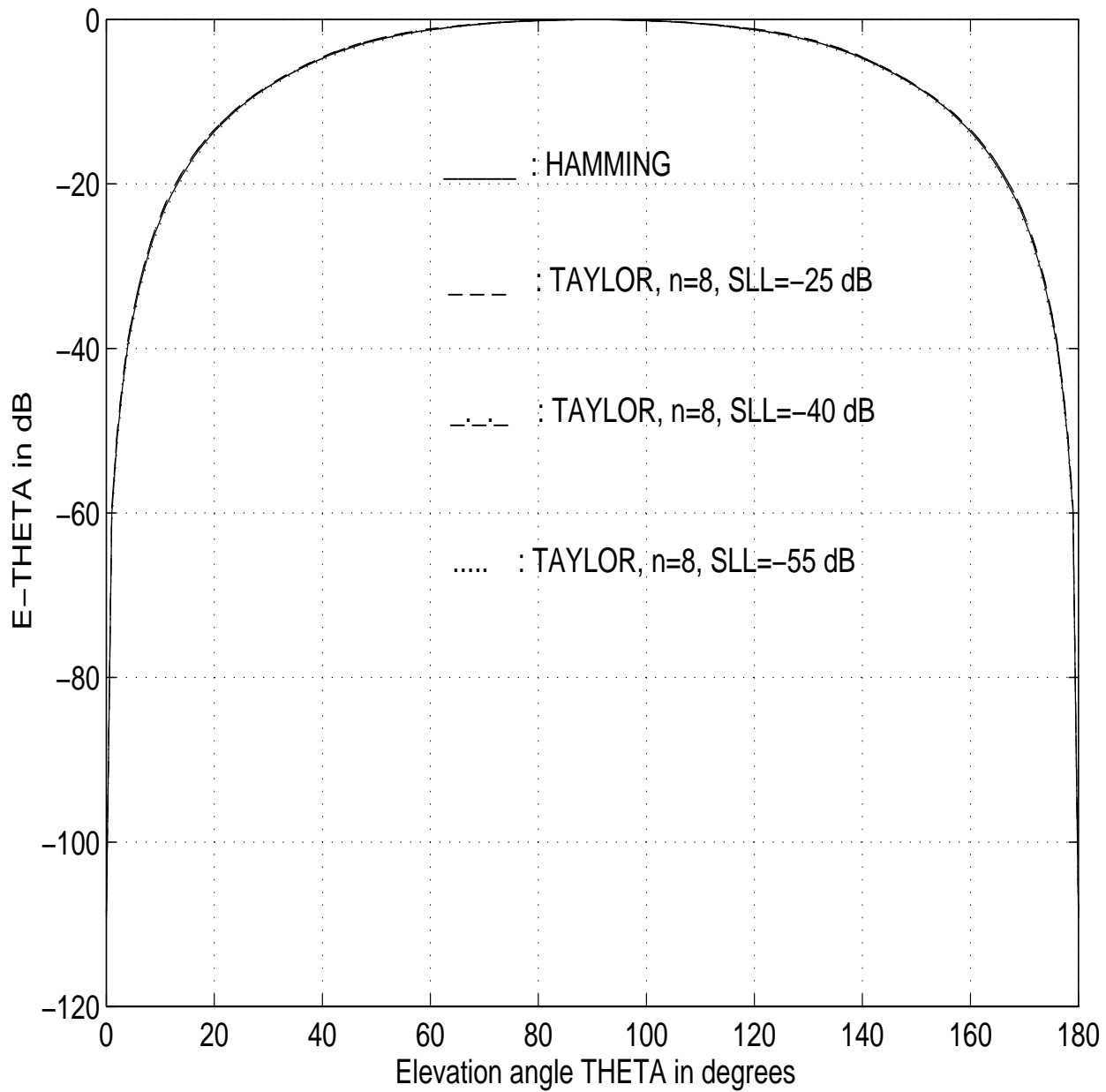
Figure 3-10: Far-field pattern comparisons between Hamming and Taylor distributions for $ka = 20$, $kh = 1.57$, $f = 5$ GHz, $\varphi_s = 120^0$, $N_{elm} = 21$ in the $\phi = 60^0$ plane. Here, $\bar{n}$ in Eq. (2.2) is designated by n.

phase taper in Eq. (2.6). In fact the sidelobe is reduced from -30 dB to -36 dB (Fig. 3-11), and the 3-dB beamwidth is reduced from 44^0 to 24^0 (Fig. 3-12) ! This is a substantial improvement that directly contributes to the improvement in adaptivity and frequency reuse in RDRN communication systems, as discussed in chapter 2. The results in Figs. 3-11 and 3-12 were repeated for other values of ka and φ_s and similar conclusions were reached.

From Fig. 3-13 one can draw similar conclusions as in Fig. 3-7. As shown in Fig. 3-14, increasing the Taylor design sidelobe causes the taper at the edge element to decrease from 0.12 (SLL=-40 dB) to 0.02 (SLL=-70 dB). It is seen from Fig. 3-15 that this change amplitude taper at the edges of the projected linear length controls the pattern of the sector. The result for Fig. 3-16 is discussed separately below.

To understand the effect of phase taper on the overall pattern, results for $\frac{s}{\lambda} \simeq 0.55$ in Figs. 3-16 and 3-5 need to be carefully examined. In Fig. 3-5 one can notice that amplitude taper produces higher sidelobes that will deteriorate the SINR. However an additional phase taper can significantly improve the pattern as shown in Fig. 3-16 for $\frac{s}{\lambda} = 0.55$. (In Fig. 3-16 this corresponds to the case of $N_{elm} = 15$.) The large sidelobes are absent in the latter case. This improvement can be attributed due to greater control of interference between the direct ray and creeping rays, as discussed in [3, p. 377], by introducing the additional parabolic (quadratic) phase taper.

The effects of various even-symmetric phase tapers on the radiation pattern are shown next. The data refers to $ka = 20$, $kh = 1.57$, $f = 5$ GHz, $\varphi_s = 120^0$ and $N_{elm} = 21$. For this configuration $\frac{s}{\lambda} = 0.36$. The results are shown in Figs. 3-17 to 3-21, and are briefly discussed here. The amplitude taper was determined from the Taylor distribution ($\overline{n} = 8$ and SLL=-55 dB) in Eq. (2.2). It maybe recalled that Eq. (2.6) was used to determine the various phase profiles.

From Figs. 3-17 and 3-18 it is clear that the parabolic profile yields better

pattern control. The triangular phase taper has the narrowest beamwidth and highest sidelobes.

The foregoing conclusion is further confirmed by the results in Figs. 3-19 to 3-21. The individual results in these figures are thus not discussed any further. One may also conclude that $2.5 < \tau < 5.0$ in Eq. (2.6) for the exponential taper should provide an optimum trade-off between beamwidth and sidelobe levels. Careful inspection of Fig. 3-17 shows that such a taper would be bounded by the parabolic and triangular distributions.

To summarize, the results in this chapter show that independent control of both amplitude and phase taper (or profile) across the elements of a cylindrical array can provide significant improvement in overall pattern. It may be concluded from Fig. 2-3 that the effects of the DBF technique are simulated by applying independent amplitude and phase control across the elements. Furthermore, for equally spaced elements along a circular array, $\frac{s}{\lambda} \leq 0.6$ produces an acceptable pattern near the boresight. From investigations by previous workers [21], it was found that mutual coupling effects become dominant when $\frac{s}{\lambda} \leq 0.4$. Selecting the inter-element spacing within this range, one can judiciously decide a trade-off between the array geometry and the performance. This information is used to propose an algorithm helpful in designing conformal arrays for RDRN applications. The numerical results also suggest that DBF techniques, as introduced in chapter 2, have the potential of providing better pattern control that can substantially improve the merits of the overall system.

3.3   Proposed Technique for Defining the Array Configuration and Excitation of Elements

The problem of defining the array geometry and determining the element excitation is outlined below. The bounds for interelement spacing $0.4 \leq \frac{s}{\lambda} \leq 0.6$ is
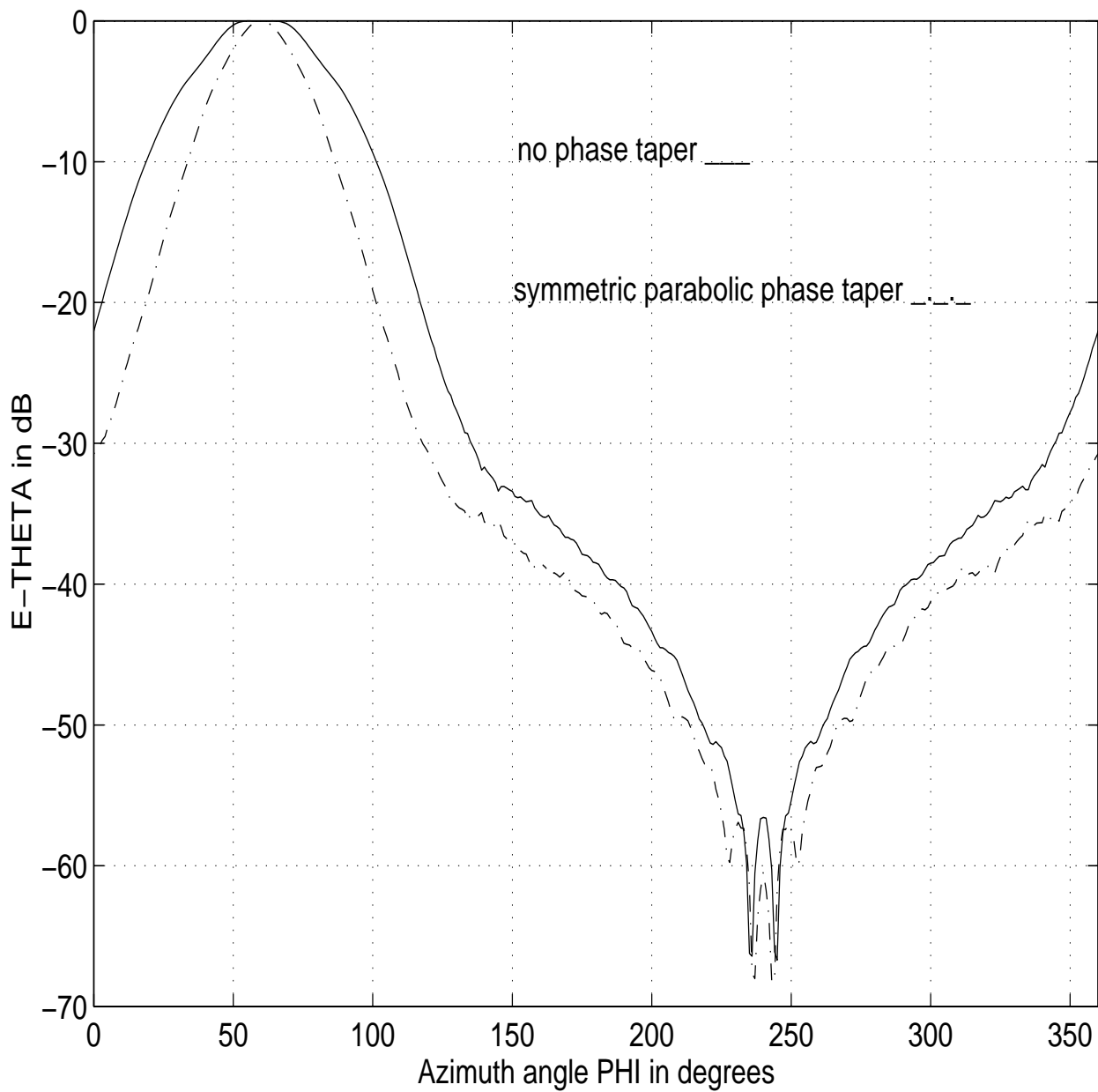
Figure 3-11: Far-field pattern comparisons between Taylor distributions for $ka = 20$, $kh = 1.57$, $f = 5$ GHz, $\varphi_s = 120^0$, $N_{elm} = 21$ and $\frac{s}{\lambda} = 0.36$ in the $\theta = 90^0$ plane; $\bar{n} = 8$ and a sidelobe level of -40 dB was assumed in Eq. (2.2). The parabolic phase taper was determined via Eq. (2.6).

33
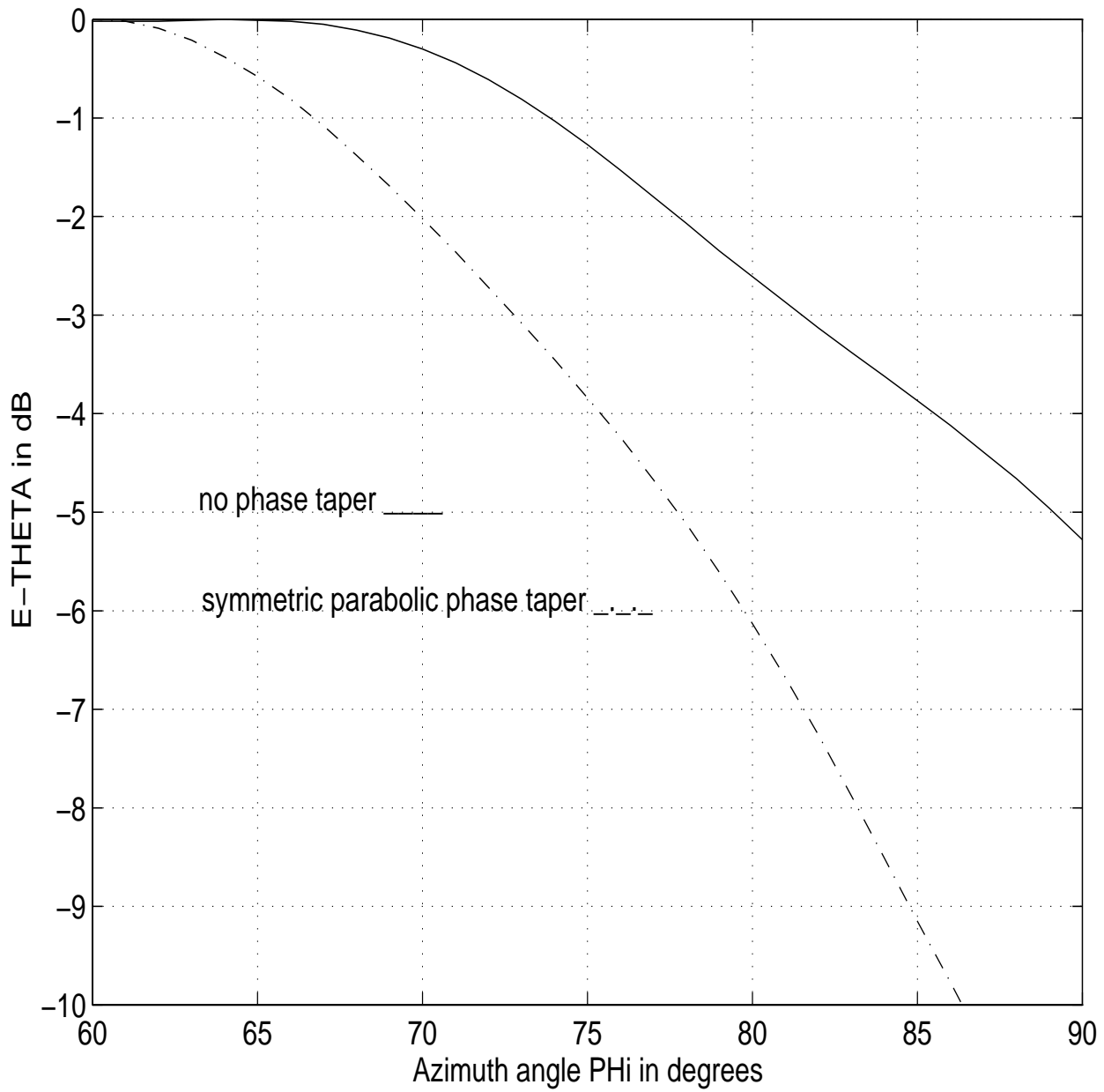
Figure 3-12: Detailed pattern comparisons for with and without phase tapers; all other data same as in Fig. 3-11. Note that only one-half of the pattern about boresight ($\Phi = 60^0$) is shown.
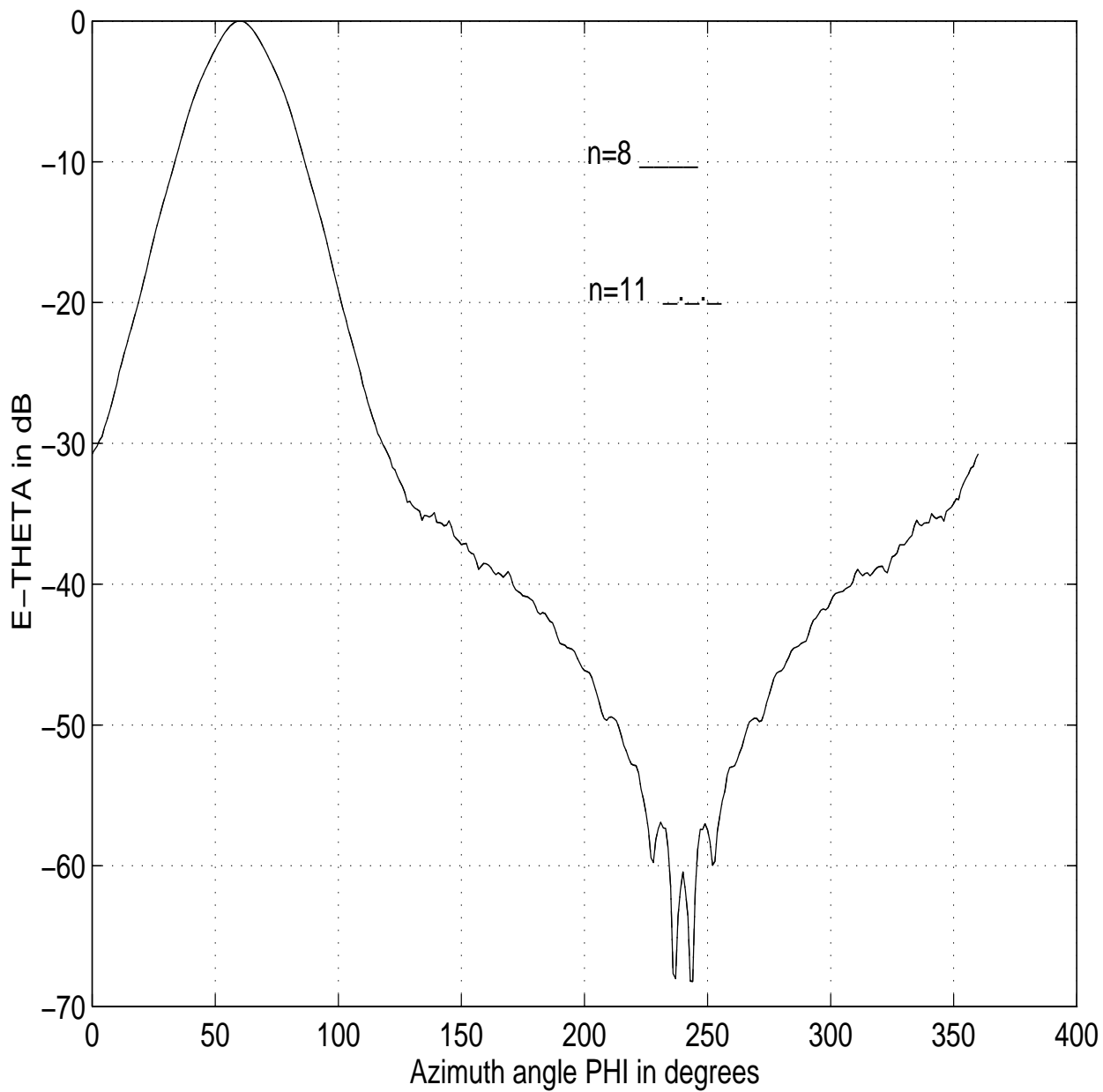
Figure 3-13: Far-field pattern comparisons between Taylor distributions for $ka = 20$, $kh = 1.57$, $f = 5$ GHz, $\varphi_s = 120^0$, $N_{elm} = 21$ and $\frac{s}{\lambda} = 0.36$ in the $\theta = 90^0$ plane. Parabolic phase taper Eq. (2.6) was used for both $\bar{n} = 8, 11$, and a sidelobe level of -40 dB was assumed in Eq.(2.2).
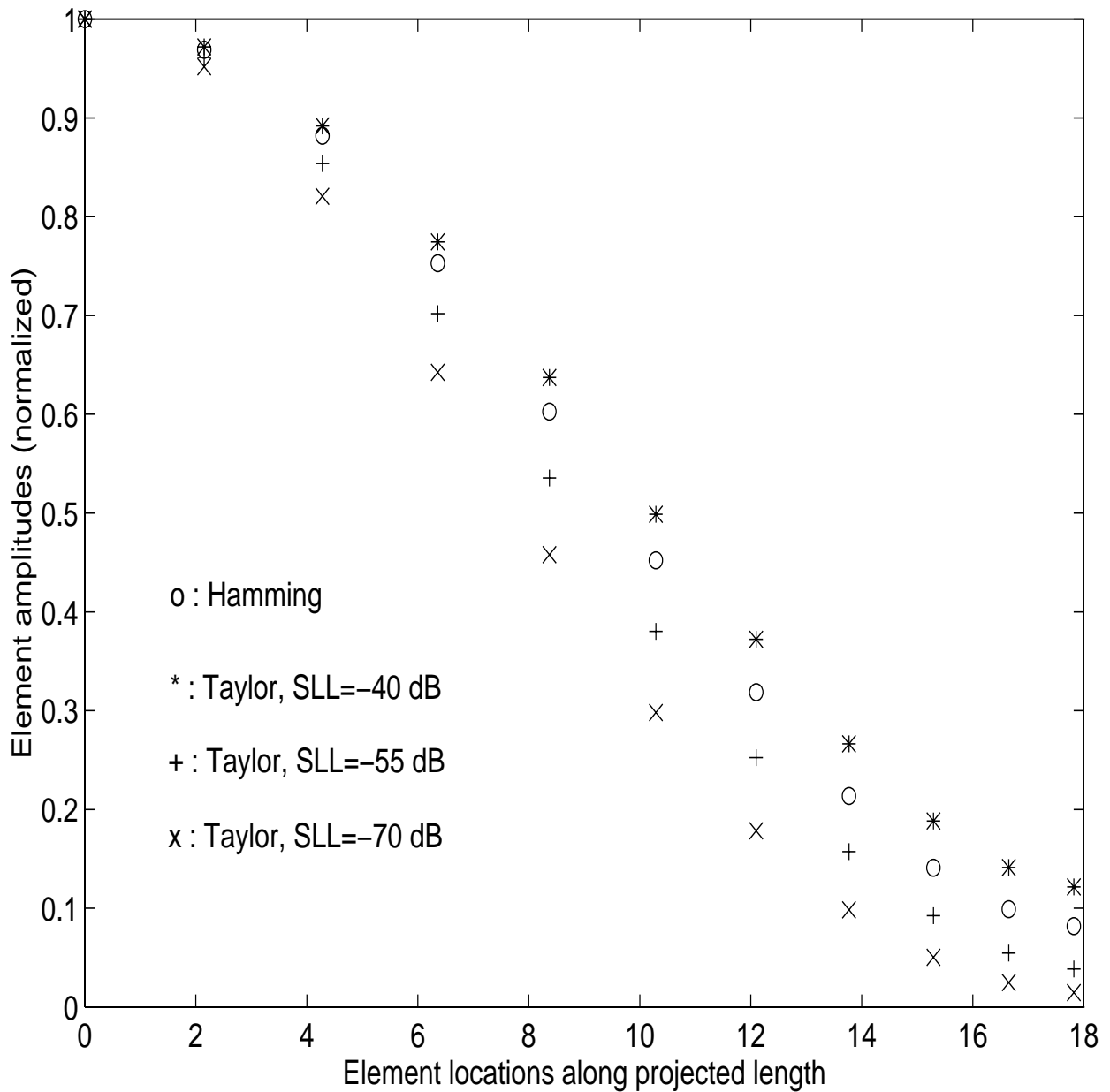
Figure 3-14: Amplitude distribution at the discrete element locations along the projected length shown in Fig. 2-4 (b). In this figure $ka = 20$,$kh = 1.57$,$f = 5$ GHz, $\varphi_s = 120^0$ and $N_{elm} = 21$. For the Taylor distribution $\overline{n} = 8$ and is designated by n in this figure. Due to even-symmetric nature of Eqs. (2.1) and (2.2), only one-half of the functions are shown.
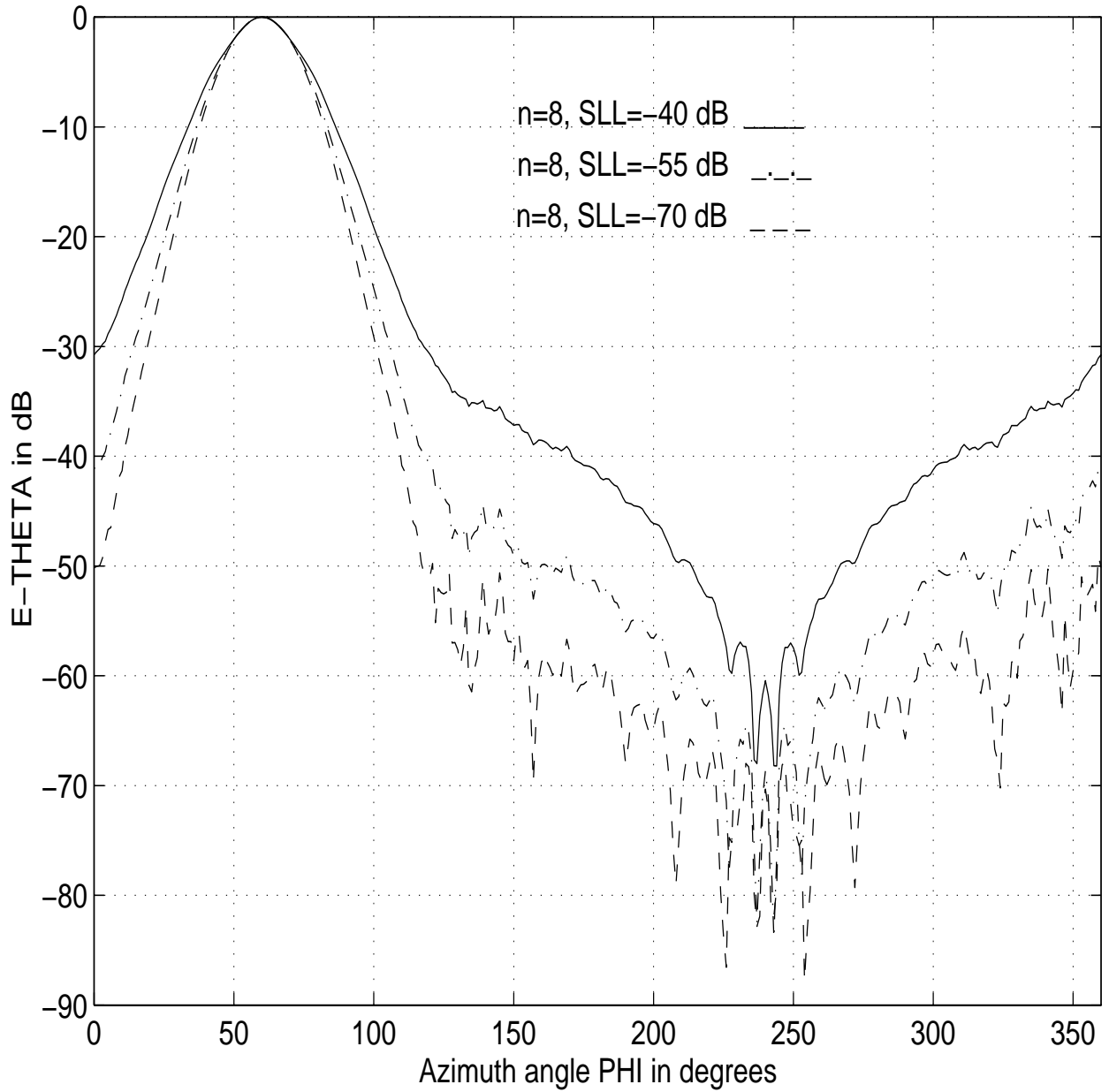
Figure 3-15: Far-field pattern comparisons between Taylor distributions for $ka = 20$, $kh = 1.57$, $f = 5$ GHz, $\varphi_s = 120^0$, $N_{elm} = 21$ and $\frac{s}{\lambda} = 0.36$ in the $\theta = 90^0$ plane. Parabolic phase taper, for all three cases, was assumed. Here $\overline{n}$ in Eq. (2.2) is designated by n.

37
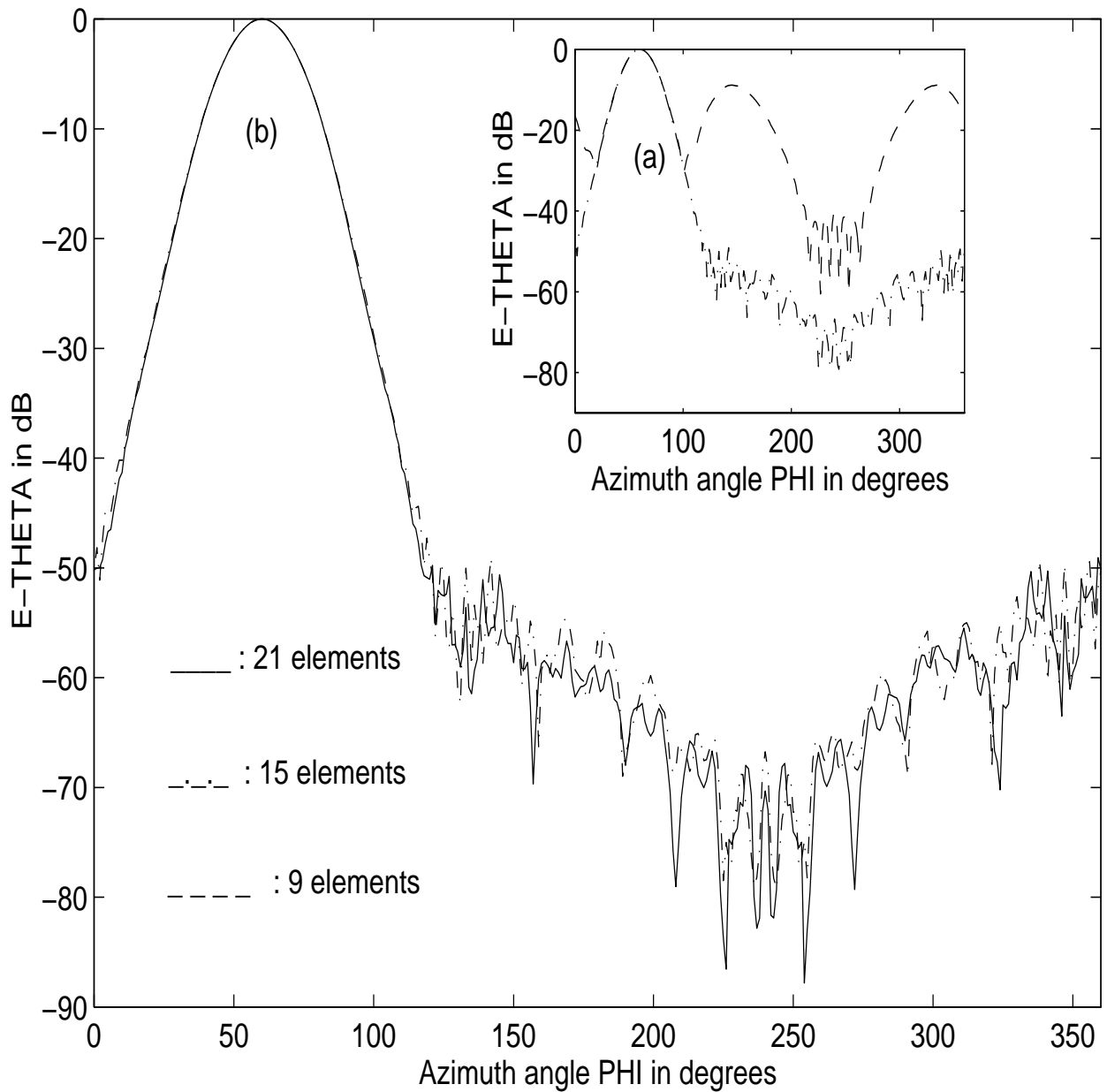
Figure 3-16: Far-field pattern comparisons between Taylor distributions for $ka = 20$,$kh = 1.57$,$f = 5$ GHz,$\varphi_s = 120^0$,$N_{elm} = 21, 15, 9$ corresponding to $\frac{s}{\lambda} = 0.36, 0.54, 0.9$,respectively, and in the $\theta = 90^0$ (azimuth) plane. Parabolic phase taper, for all three cases, was assumed. Here $\overline{n} = 8$ and a design sidelobe level of -70 dB was used in Eq. (2.2).

38
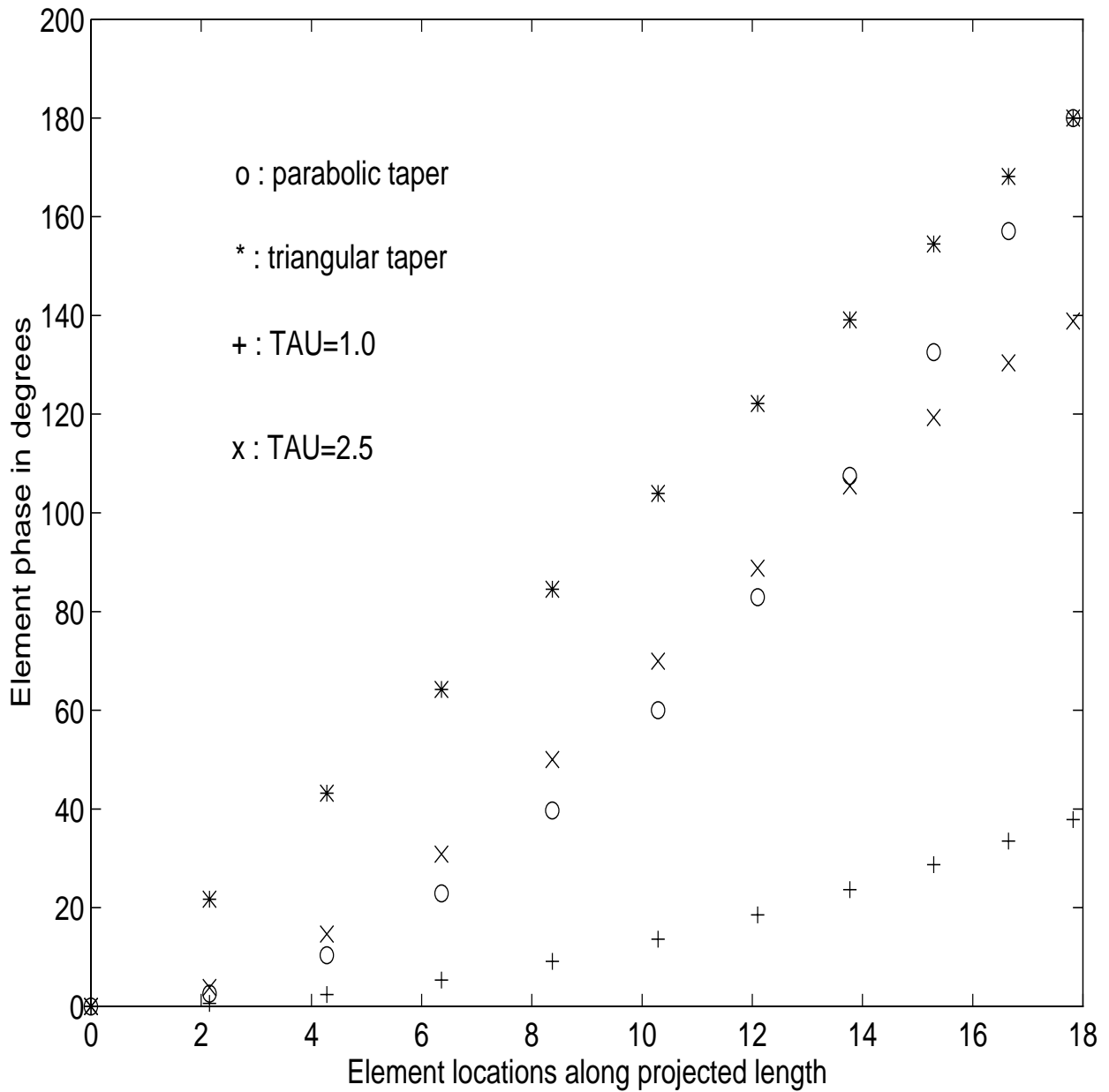
Figure 3-17: Phase distribution at the discrete element locations along the projected length shown in Fig. 2-4 (b). Eq. (2.6) was used to generate the results shown here for $ka = 20$, $kh = 1.57$, $f = 5$ GHz, $\varphi_s = 120^0$ and $N_{elm} = 21$; τ in Eq. (2.6) is designated here by TAU.
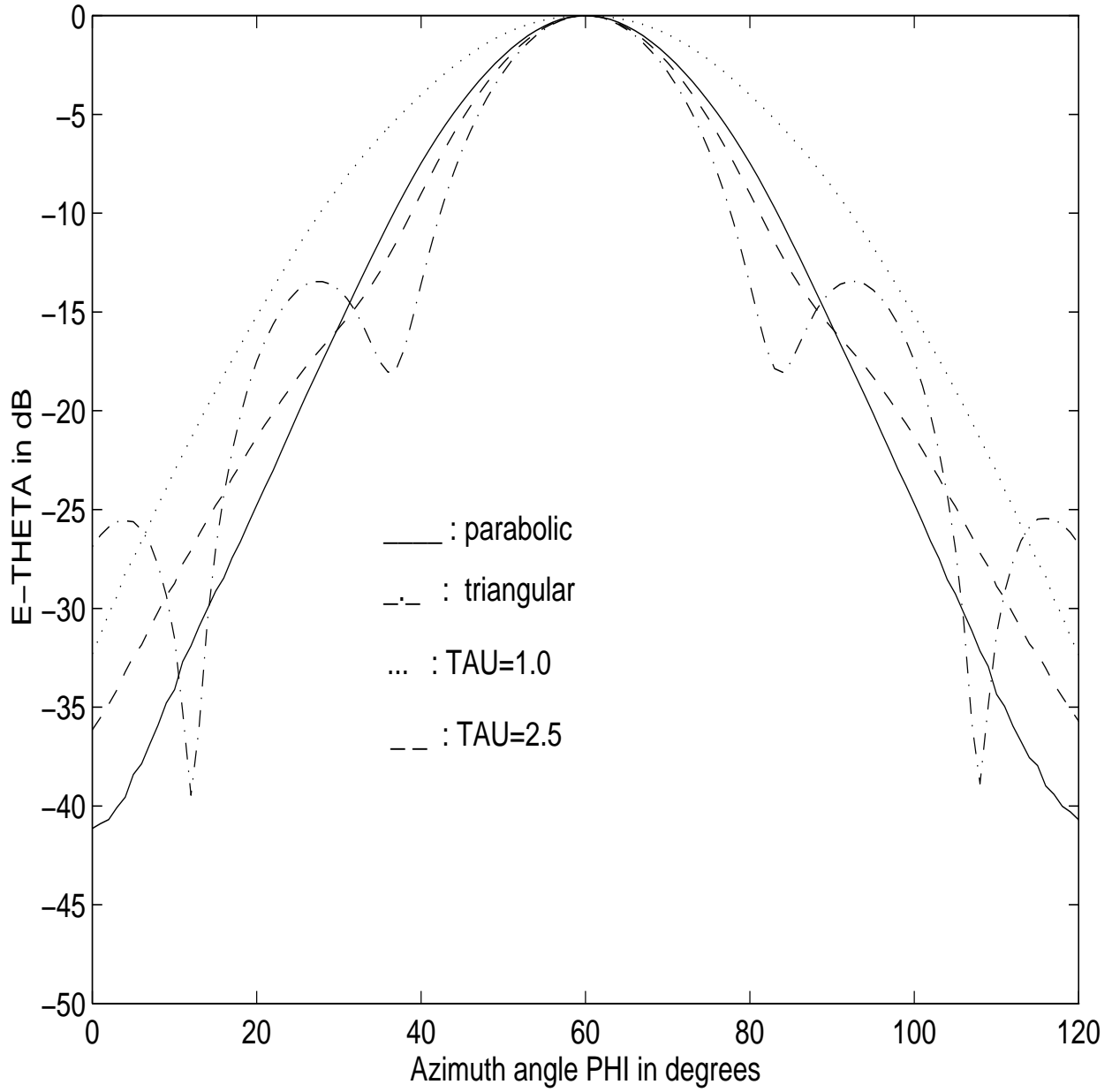
Figure 3-18: Comparison of far-field patterns for the four different phase tapers in Fig. 3-17. The pattern boresight (mainbeam maxima) is at $\Phi = 60^0$ and other data are identical to the ones in Fig. 3-17.
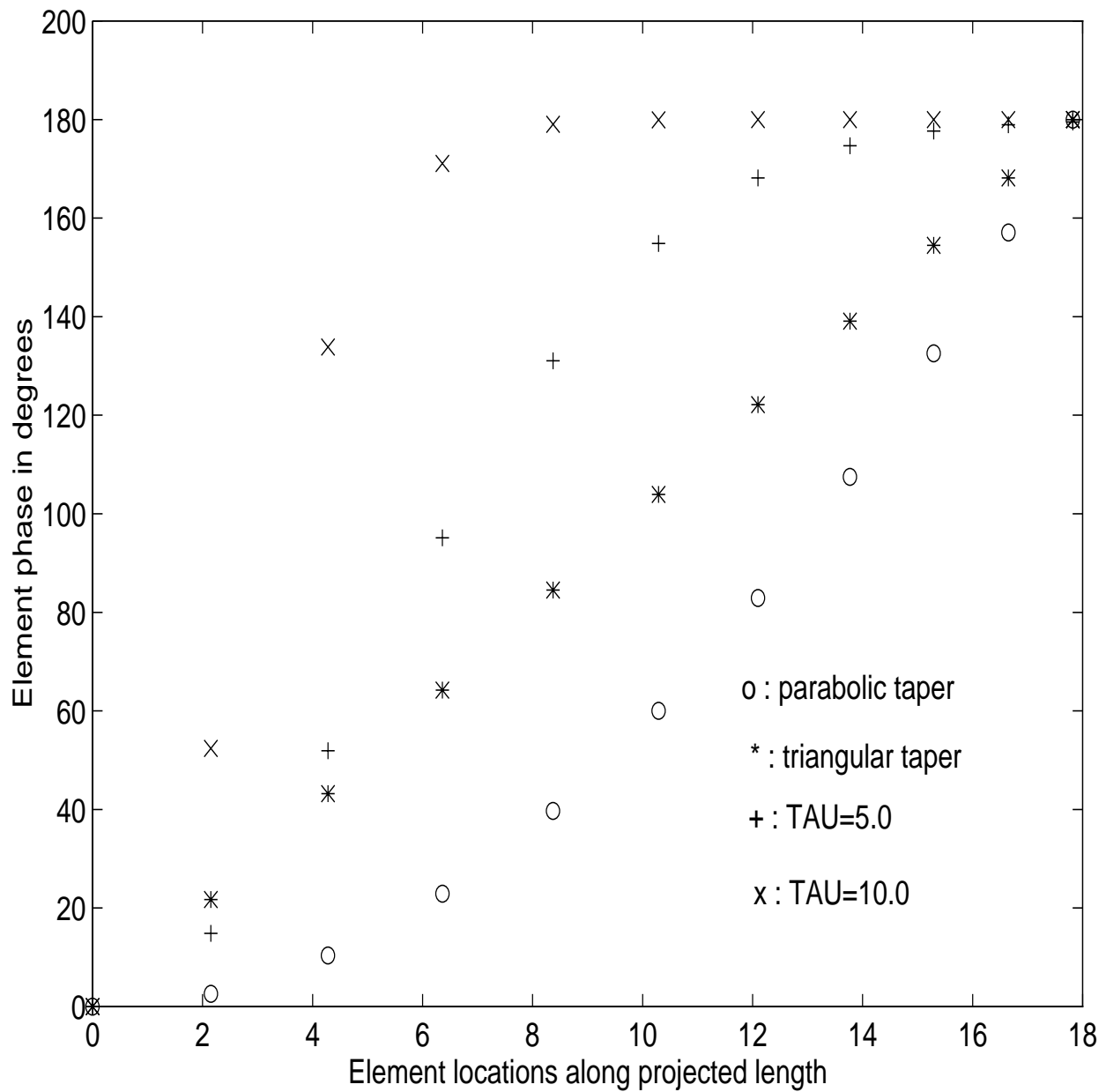
Figure 3-19: Phase distribution at the discrete element locations along the projected length shown in Fig. 2-4 (b) . Eq. (2.6) was used to generate the results shown here for $ka = 20, kh = 1.57, f = 5$ GHz, $\varphi_s = 120^0$ and $N_{elm} = 21$; τ in Eq. (2.6) is designated here by TAU.
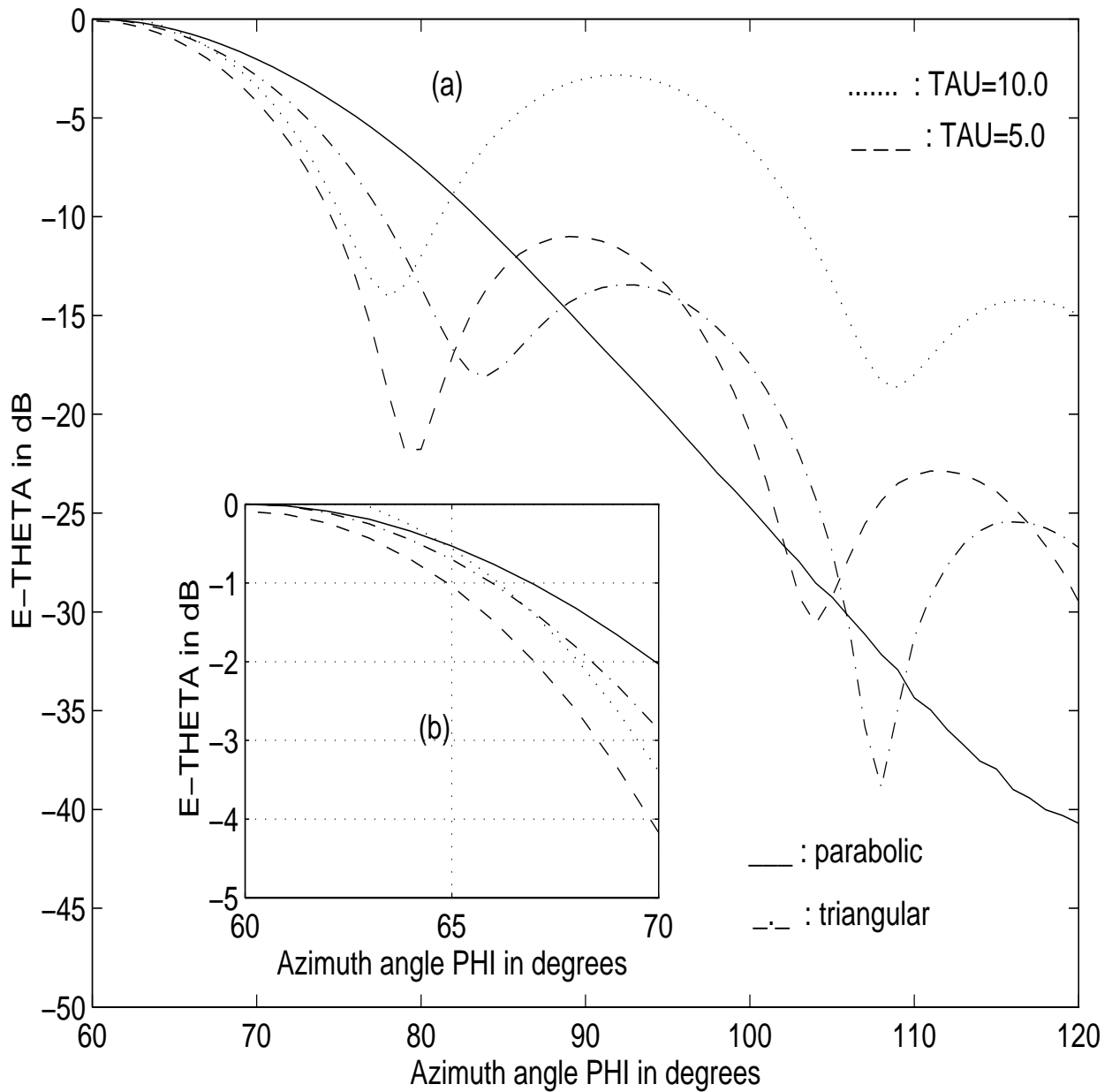
Figure 3-20: Comparison of far-field patterns for the four different phase tapers in Fig. 3-19. The pattern boresight (mainbeam maxima) is at $\Phi = 60^0$ and other data are identical to the ones in Fig. 3-19. The 3-dB beamwidth comparison is shown in detail in inset (b). A Taylor distribution across the elements, for $\bar{n} = 8$ and a design sidelobe level of -55 dB, for all cases, was used in Eq. (2.2).

42
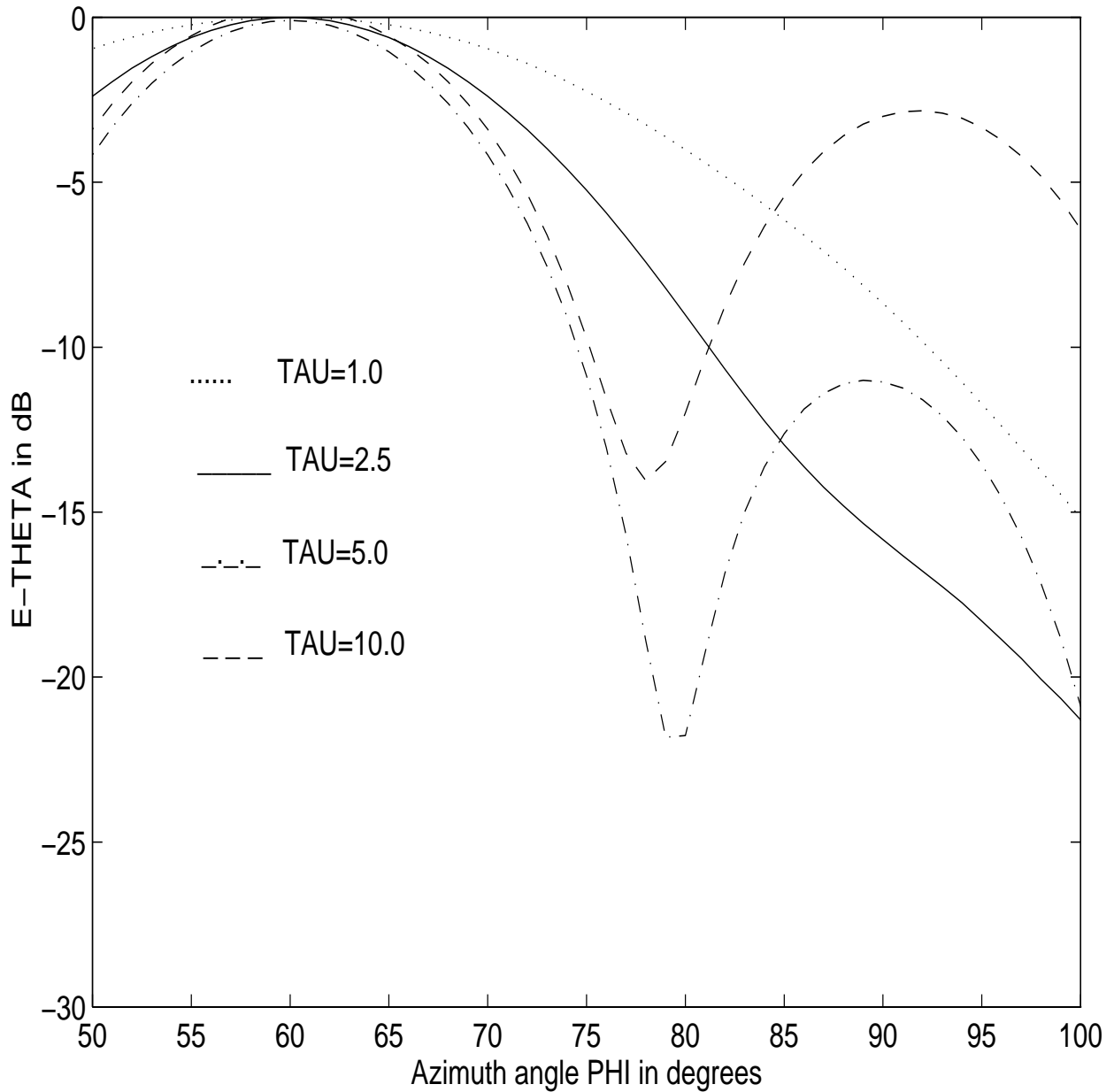
Figure 3-21: Comparison of far-field patterns for the four different values of τ (designated here by TAU) in Eq. (2.6). The pattern boresight (mainbeam maxima) is at $\Phi = 60^0$, and $ka = 20$, $kh = 1.57$, $f = 5$ GHz, $\varphi_s = 120^0$ and $N_{elm} = 21$ here. A Taylor distribution across the elements, for $\overline{n} = 8$ and a design sidelobe level of -55 dB, for all cases, was used in Eq. (2.2).

43

used to determine the number of elements N_{elm} in an angular sector φ_s. In this algorithm the amplitude excitations are determined via Taylor distribution since it provides a functional relationship between array length (linear), beamwidth and sidelobe-level, allowing more flexibility in examining tradeoffs between such parameters. For the purposes of design, the Taylor parameter $\overline{n}$ in (2.2) can be selected between 8 and 11 as suggested in [3]. The formulas presented here for determining the array geometry and element excitations have been obtained from [3] and [13].

The main procedure comprises of two steps:

(a) Determine array geometry and the total number of elements N_{total} in the array

(b) Once the array geometry is defined, determine the complex excitations according to the degree of pattern control

These two aspects are elaborated below.

For part (a) determine the cylinder radius given the minimum bandwidth from

$$\frac{\Delta f}{f_0} = \frac{\pi}{4ka}.$$

(3.1)

In (3.1) $k = \frac{2\pi}{\lambda}$ is the free-space wavenumber, f_0 the carrier frequency and Δf the instantaneous bandwidth. If the minimum beamwidth θ_{min} and the sidelobe SLL (in dB) are specified then compute

$$R = 10^{-\frac{SLL}{20}},$$

(3.2)

and

$$A = \frac{1}{\pi} \cosh^{-1} R.$$

(3.3)

44

Next, determine beam-broadening factor

$$\sigma = \frac{\overline{n}}{\sqrt{A^2 + (\overline{n} - \frac{1}{2})^2}}. \qquad (3.4)$$

Lastly, determine the projected linear length, kL_a, by solving iteratively the following transcendental equation

$$\theta_{min} = 2\sin^{-1}\left[\frac{2\sigma}{kL_a}\left([\cosh^{-1} R]^2 - [\cosh^{-1}\frac{R}{\sqrt{2}}]^2\right)^{\frac{1}{2}}\right]. \qquad (3.5)$$

Once kL_a is found, determine the cylinder size via $2ka = kL_a$. It is obvious that (3.1) is simpler compared to (3.5).

To determine the total number of elements in the array, determine the angular increment $\Delta\phi \equiv \phi_{inc}$ from the pre-selected value of $\frac{s}{\lambda}$; compute the nearest integer from $N \times \Delta\phi = \pi$. The total number of elements in the array is given by $N_{total} = 2 \times N$.

The next problem in part (b) is to define the array sector for a given beamwidth and sidelobe level at a given scan angle ϕ_s. The geometry is shown in Fig. 3-22. The boresight, assuming symmetric pattern, can be defined as shown there. (This means that the sector should form a mainbeam maxima at ϕ_s.)

Once the boresight direction is determined the beamwidth θ_{3dB} and sidelobe level need to be specified. These two principal specifications dictate the pattern shape desired along the direction ϕ_s. From these specifications, the corresponding projected linear array length kL_a can be determined via Eqs. (3.2) to (3.5). From the geometric relation, $2a\cos\frac{\varphi_s}{2} = L_a$, which is self-evident from Fig. 3-22, one can determine the angular sector of excitation φ_s. From our earlier knowledge of $\Delta\phi$, one can use (2.5) to compute the total number of elements N_{elm} in the sector φ_s. Once N_{elm} is known y_m can be found from (2.4). The complex excitations $(w_n = M_n e^{j\alpha_n})$, across each of the N_{elm} elements, can be determined from the relevant equations in chapter 2.

BORESIGHT

Y

Projected linear
length L_a

ϕ_s

X

a

φ_s $: L_s = a \times \varphi_s$
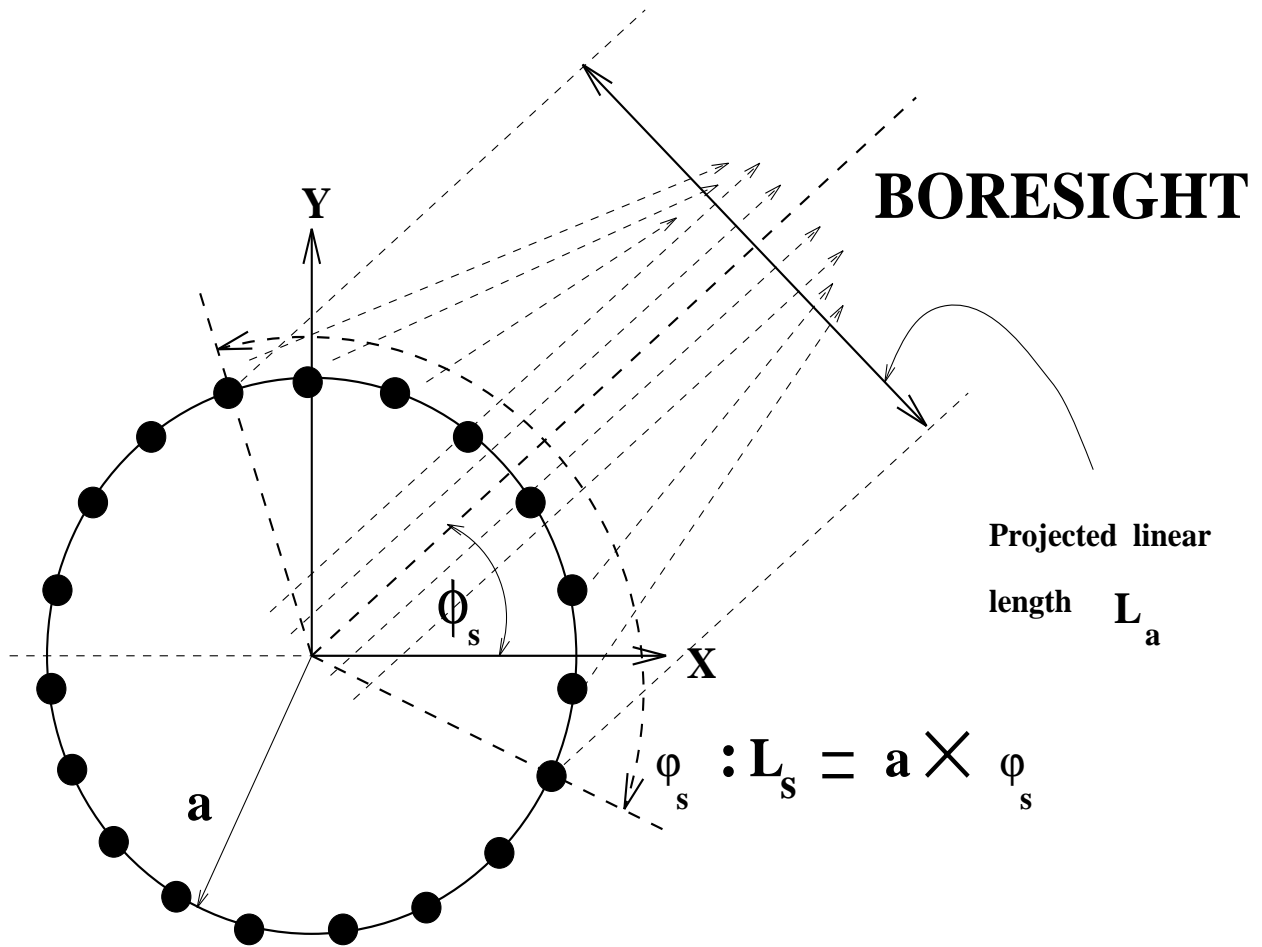
● **Elements of the Conformal Array**

ϕ_s **Beamsteering angle**

Figure 3-22: Beamforming with a cylindrical array of equispaced sources.

The foregoing discussion assumed that an even symmetric pattern is formed at the boresight of the array in Fig. 3-22. However, the rigorous proceedure is to employ the algorithms in [17],[23] for realizing an arbitrary pattern topography.

Chapter 4

Continuing and Future Investigations

4.1 Introduction

In this chapter, the present and future investigations are outlined. The emphasis is on evaluation of the proposed DBF technique. In section 4.2 the list of main tasks, that are currently being undertaken, is outlined. In section 4.3 the goals for future investigations are listed.

It is to be noted that since emphasis will be placed on numerical modeling of the antenna, many intermediate issues related to validity of the relevant formulations need to be examined. These issues cannot be addressed here since validation of formulations is an open-ended problem.

4.2 Continuing Investigations

(1) Currently completing the far-field pattern calculations for the 4-sided planar array using the NEC-BSC code. The geometry of the two configurations is shown in Fig. 4-1. The objective is to compare the architecture of the two

48

structures based on their respective far-field patterns in the azimuth $\theta = 90^0$ plane.

(2) The effects of mutual coupling will be addressed next. The pattern of the cylindrical array has been shown in this report without mutual coupling. The mutual coupling will be computed using the avaliable NEC-MM (Method of Moments) code. The dipole currents can then be used as input to the NEC-BSC code for further analysis. At this stage it is not very clear whether both the structures in Fig. 4-1 will be analyzed; this decision will depend on the analysis of results in (1).

(3) For the two geometries in Fig. 4-1, the effects of the link characteristics need to be quantified. It is important to know how the effects of the environment can alter the RDRN antenna pattern. These have not been studied in this report, but their effects are important for a proper numerical "calibration" of the antenna. To that end, the advanced version of NEC-BSC code (version 3) will be used. This version contains sophisticated ray-tracing algorithms and appropriate quasi-optic formulations [25],[26], to compute the total field at any mobile/ stationary location. Additional graphics facility and menu-driven functions allow rapid identification of the interference ray paths which cause fading.

(4) The important aspect of adaptivity and beamsteering will be studied. The numerical algorithms [17],[23] that determine the complex excitations, will be implemented. This will be followed by analyzing techniques that allow multiple beam generation in adaptive arrays.

At this stage, items (1) and (2) are given top priority.

The issues itemized above generally address all the important topics associated with conventional array antennas. It is expected that extensive use of NEC codes will be necessary to complete the above tasks. Again, several amplitude and phase

49

1. Cylindrical array of half-wave dipoles.

**2. Multi-face planar array of half-wave dipoles**
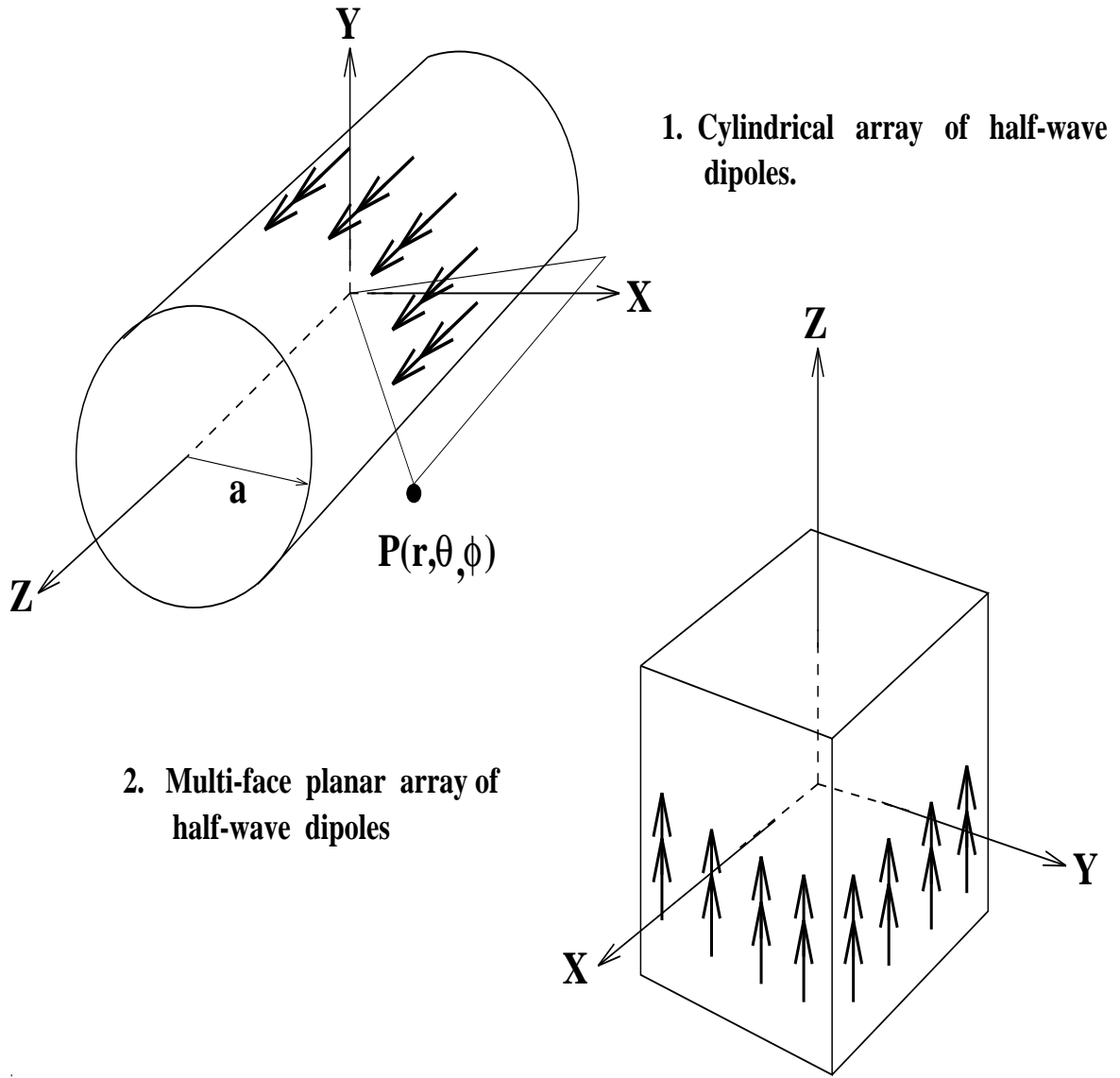
Figure 4-1: Two important array antenna configurations that can be analysed using NEC-Basic Scattering Code.

tapers will be studied, in order to critically examine the concept of applying the DBF technique to conformal arrays. The information gleaned from these investigations will be used in augmenting the array algorithm proposed in section 4.2.

4.3 Future Investigations

For advanced applications, the conformal microstrip patch array in Fig. 2-2 needs to be analysed in detail. It appears from the recent investigations that there is a paucity of efficient numerical algorithms for a full-wave analysis of the array [18]-[20]. It is suggested that future work should proceed towards developing efficient algorithms in analysing the conformal microstrip array. The results in (1)-(4) will either be used as benchmarks in developing these algorithms or may be incorporated in the full-wave analysis of conformal microstrip antennas.

From the investigations reported in the earlier chapters, it appears that for the geometry in Fig. 2-2 the mutual coupling remains to be analysed. This is because the mutual coupling for an array depends strongly on the local environment which is a part of the antenna. For example, the far-field patterns of a $\frac{\lambda}{2}$, electric dipole and a rectangular microstrip patch, excited in their respective dominant modes, appear similar, since they do not depend strongly on the local environments. However, the input impedances of these two antennas are markedly different. This is becausethe microstrip antenna excites additional leaky and surface waves which control the input and mutual impedances [34]. These waves are excited due to the presence of the grounded dielectric substrate. For the case of a $\frac{\lambda}{2}$ electric dipole, radiating in free-space, such waves are absent. Consequently modeling of impedance behavior is specific to the geometry of the antenna. Furthermore, modeling of impedance behavior of an array gives information about multichannel operation in wireless systems [1].

Chapter 5

Summary and Conclusions

A cylindrical, Digital BeamForming (DBF) array of rectangular microstrip patches has been proposed for futuristic RDRN (Rapidly Deployable Radio Network) communication systems. The circular geometry of the array provides 360^0 coverage in the azimuth plane. The DBF technique allows for independent amplitude and phase control of elements in arrays, resulting in high-degree of pattern control. Each individual element in a DBF array has a pair of transmitter and receiver which significantly increases the total number of degrees of freedom in the signal, compared to a conventional phased array. This flexibility allows simultaneous generation of multiple beams, each with different information. A comparison between a DBF and an electronically scanned phased array is planned for future work.

To simulate the DBF technique, the effects of amplitude and phase tapers were studied for the canonical model of an array of axial, $\frac{\lambda}{2}$ dipoles in presence of a conducting circular cylinder. The results of this preliminary analysis of the array does not consider mutual coupling. Rigorous numerical analysis of mutual coupling, reported by earlier investigators, indicate that interelement spacings less than 0.4λ should be avoided to obtain reasonable pattern control. Analysis of the far-field patterns showed that an upper of limit of 0.6λ should be placed on the inter-element spacing betwen elements. Increasing the inter-element spacing

beyond this value results in higher peaks similar to the appearence of grating lobes in a linear array. Since the inter-element spacing depends on cylinder radius ka, the angular span of the sector φ_s, and the number of elements N_{elm} in φ_s, one may use the above limits in designing the array geometry.

It was found that far-field patterns with both amplitude and phase taper yielded narrower beamwidths and lower sidelobes when compared to patterns generated by using amplitude taper only. Analysis of the far-field patterns for a class of even-symmetric phase distribution showed that an optimum phase distribution for improved pattern control is the one which is bounded by the parabolic (quadratic) and triangular (linear) phase profiles. This result is interesting for RDRN applications since low-sidelobe, narrow-beamwidth arrays reduce multipath effects and hence can improve the diversity of the communication system. Such a feature allows secure transmission and reception of signals, desirable to the end user. Our preliminary results seem to indicate that controlling the complex excitations in a DBF array can generate narrow beams and lower sidelobes. However, additional investigations are necessary to examine these issues more fully. Finally, an algorithm to determine the array geometry and excitation has also been proposed here.

The numerical comparsion between a cylindrical and multi-face planar array is currently being investigated. These studies will help in providing additional information on architectures of several candidate systems. The effects of adaptivity and link topology on pattern performance will also be reported in future investigations.

Bibliography

[1] K. Fujimoto, J. R. James (eds.), *Mobile Antenna Systems Handbook*, Artech House, Boston, MA, USA, 1994.

[2] A. Kumar, *Fixed and Mobile Terminal Antennas*, Artech House, Boston, MA, USA, 1991.

[3] R. J. Mailloux, *Phased Array Antenna Handbook*, Artech House, Boston, MA, USA, 1994.

[4] K. S. Shamnugan *et. al.*, "Investigation of Algorithms for a Spatially Adaptive Antenna," technical report TISL-5481-1, Telecommunications and Information Sciences Laboratory, Center for Research, Inc., University of Kansas, November 1985.

[5] K. S. Shanmugan *et. al.*, "Rapidly Deployable Radio Network (RDRN): Semi-Annual Technical Report," technical report TISL-10920-08, Telecommunications and Information Sciences Laboratory, University of Kansas, Lawrence, June 1995.

[6] R. C. Compton, *Adaptive Antennas: Concepts and Performance*, Prentice Hall, Englewood Cliffs., NJ, USA, 1988

[7] H. Steskyal, "Digital Beamforming Antennas (An Introduction)," *Microwave Journal*, pp. 107-122, January 1987.

[8] S. Inatsune *et. al.*, "Digital Beamforming Using a Planar Array," *Proceedings of the International Symposium on Noise and Clutter Rejection in Radars and Imaging Sensors*, T. Suzuki, H. Ogura and S. Fujimura eds., Japan, 1989.

[9] H. Steskyal and J. S. Herd, "Mutual Coupling Compensation in Small Array Antennas," *IEEE Trans. Antennas Propagat.*, vol. 38, no. 12, pp. 1971-1975, December 1990.

[10] L. J. Ricardi, "Multiple Beam Antennas," chapter 6 in the *Handbook of Antenna Design*, vol. 1, A. W. Rudge, K. Milne, A. D. Olver and P. Knight eds., Peter Peregrinus Ltd., London, UK, 1982.

[11] G. V. Borgiotti, "Conformal Arrays," Chapter 11, vol. 2, *ibid.*

[12] M. I. Skolnik, *Introduction to Radar Systems*, McGraw-Hill Book Company, NY, USA, 1980.

[13] W. L. Stutzman and G. A. Thiele, *Antenna Theory and Design*, John Wiley and Sons, NY, USA, 1981.

[14] I. J. Gupta and A. H. Ksienski, "Dependence of Adaptive Array Performance on Conventional Array Design,"*IEEE Trans. Antennas Propagat.*, vol. AP-30, no. 4, pp. 549-553, July 1982.

[15] I. J. Gupta and A. H. Ksienski, "Effect of Mutual Coupling on the Performance of Adaptive Arrays,"*IEEE Trans. Antennas Propagat.*, vol. AP-31, no. 4, pp. 785-791, September 1983.

[16] D. F. Kelly and W. L. Stutzman,"Array Antenna Pattern Modeling Methods That Include Mutual Coupling Effects,"*IEEE Transactions on Antennas and Propagation*, vol. 41, no. 12, pp. 1625-1634, December 1993.

[17] R. Vescovo, "Constrained and Unconstrained Synthesis of Array Factor for Circular Arrays,"*IEEE Trans. Antennas Propagat.*, vol. AP-43, no. 12, pp. 1405-1410, December 1995.

[18] A. Nakatani *et. al.*, "Accurate Green's Function Computation for Printed Circuit Antennas on Cylindrical Substrates,"*Electromagnetics Journal*, no. 6, pp. 243-254, 1986.

[19] A. Nakatani and N. G. Alexopoulos, "Microstrip Elements on Cylindrical Substrates - General Algorithm and Numerical Results,"*Electromagnetics Journal*, no. 9, pp. 405-426, 1989.

[20] A. Nakatani, "Microstrip Antennas on Cylindrical Substrates," Ph.D. dissertation, Department of Electrical Engineering, University of California at Los Angeles, 1988.

[21] J. C. Herper, A. Hessel and B. Tomasic, "Element Pattern of an Axial Dipole in a Cylindrical Phased Array, Part I: Theory," *IEEE Trans. Antennas Propagat.*, vol. AP-33, no. 3, pp. 259-272, March 1985.

[22] J. C. Herper, A. Hessel and B. Tomasic, "Element Pattern of an Axial Dipole in a Cylindrical Phased Array, Part II: Element Design and Experiments,"pp. 273-278, *ibid.*

[23] S. R. Nagesh and T. S. Vedavathy, "A Procedure for Synthesizing a Specified Sidelobe Topography Using an Arbitrary Array,"*IEEE Trans. Antennas Propagat.*, vol. AP-43, no. 7, pp. 742-745, July 1995.

[24] J. R. Wait, *Electromagnetic Radiation from Cylindrical Structures*, Peter Peregrinus, London, UK, 1988.

[25] P. H. Pathak, "High Frequency Techniques for Antenna Analysis," *Proceedings of the IEEE*, vol. 80, no. 1, pp. 44-65, January 1992.

[26] E. H. Newman and R. J. Marhefka, "Overview of MM and UTD Methods at The Ohio State University," *Proceedings of the IEEE*, vol. 77, no. 5, pp. 700-708, May 1989.

[27] S. Y. Tan and H. S. Tan, " UTD Propagation Model in an Urban Street Scene for Microcellular Communications," *IEEE Trans. Electromag. Compatibility*, vol. EMC-35, no. 4, pp. 423-428, November 1993.

[28] G. A. J. van Dooren and M. H. A. J. Herben, "A Deterministic Approach for the Modeling of Wave Propagation around Buildings," *Journal of Electromagnetic Waves and Applications*, vol. 8, no. 2, pp. 175-194, 1994.

[29] R. J. Marhefka and W. D. Burnside, "Numerical Electromagnetics Code - Basic Scattering Code," NEC-BSC (version 2), Part 1: User's Manual, The Ohio State University, ElectroScience Laboratory, Columbus, Ohio, Technical Report no. 712242-14, December 1982.

[30] D. Chatterjee, "Evaluation of a Class of Creeping Wave Formulations with Applications to Practical Modeling of Aircraft Antenna EMI Coupling Problems," M.A.Sc thesis, Department of Electrical and Computer Engineering, Concordia University, Montréal, Québec, Canada, March 1992.

[31] D. Chatterjee and R. G.Plumb, "A Hybrid Formulation for the Probe-to-Patch Attachment Mode Current for Rectangular Microstrip Antennas, to appear in May 1996 issue of the *IEEE Transactions on Antennas and Propagation*.

[32] D. Chatterjee and R. G. Plumb, "Comparison of Antenna Architectures for Rapidly Deployable Radio Networks (RDRN) based on Far-Field Pattern Performance," accepted for presentation at *IEEE Antennas and Propagation and URSI/UNSC Symposium* to be held at Maryland, July 21-26, 1996.

[33] D. Chatterjee and R. G. Plumb, "Modeling Far Field Patterns of Cylindrical Arrays for Rapidly Deployable Radio Networks (RDRN) Using the NEC-Basic Scattering Code," accepted for presentation at *IEEE Antennas and Propagation and URSI/UNSC Symposium* to be held at Maryland, July 21-26, 1996.

[34] D. Chatterjee, "Advances in Modeling Techniques For a Class of Microstrip Antennas," Ph.D. Dissertation in progress.

Appendix A

Validation of Formulations in NEC-BSC2 Code.

The results presented in this appendix indicate the validity of the NEC-BSC code. The NEC-BSC code contains high-frequency formulation [25] which itself is approximate. Consequently it is advisable to know the limitations of the applications of NEC-BSC to practical modeling problems. To that end, a canonical model was selected which can be modeled by the NEC-BSC code and also by rigorous analysis. For single, axial, electric dipole one obtains from [24, p. 27] the dominant far-zone component for electric field is

$$E_\theta \simeq \frac{\jmath \mu \omega e^{-\jmath kr}}{4\pi r} \sin\theta \left[\int_a^b i(\tau) e^{\jmath k\tau \cos\theta} d\tau \right] \times \Psi(\theta, \phi), \qquad (A.1)$$

when it is radiating in presence of a conducting circular cylinder. In (A.1)

$$\Psi(\theta, \phi) = \sum_{m=0}^{\infty} \epsilon_m \cos(\phi - \phi_0) e^{\frac{\jmath m\pi}{2}} \left[J_m(k\rho_0 \sin\theta) - H_m^{(2)}(k\rho_0 \sin\theta) \frac{J_m(ka \sin\theta)}{H_m^{(2)}(ka \sin\theta)} \right].$$
$$(A.2)$$

The dipole is considered located in the x-y plane at (ρ_0, ϕ_0), where $\rho_0 = a + h$. In (A.1) and (A.2) (r, ϕ, θ) are the coordinate locations in the far-field; $i(\tau)$ in (A.1)

57

is the current along the dipole antenna whose endpoints are at $\tau = a$ and $\tau = b$. In (A.2) $J_m(\cdots), H_m^{(2)}(\cdots)$ designate the standard Bessel and Hankel functions, and ϵ_m is the Neumann number defined in [24, p. 25]. It is emphasized that (A.1) and (A.2) are rigorous solutions to the canonical problem in the far zone.

Suppressing the r-dependence and for $\theta = 90$, one notices that only $\Psi(\theta, \phi)$ will be the contributing term in (A.1). This special form was used to compare against the results from NEC-BSC code. The NEC-BSC code contains asymptotic formulations that are numerically very efficient when $ka \to \infty$. The only way to understand limitations of the formulations of NEC-BSC code is to compare them against the exact solution for the same canonical problem. The results are shown in Figs. A-1 to A-4. In regions where $\Phi \geq 120^0$, the agreement is not good. The reason is that the infinite series requires a lot of terms for convergence for $ka \geq 10$ in these regions in physical space. This means that at every value of Φ exceeding 120^0, the series requires more number of terms for its convergence. The overall agreement is reasonable considering that only 16 terms that are taken for eigenfunction computations. The reason for this slow convergence is that the Hankel functions converge very slowly when the observation point in the far-zone and in the angular regions for which $\Phi \geq 120^0$.

Comparing Figs. A-1 and A-2 one notices that the better agreement betwen the eigenfunction and NEC-BSC code when $k\rho_0 = 9.57$. This value corresponds to $h = \frac{\lambda}{4}$ in Fig. 2-5. Similar conclusions can be reached by examining the result in A-3. In Fig. A-4 one notices ripples in the eigenfunction result from (A.2) even when $\Phi << 120^0$. This is unlike the results in Figs. A-1 to A-3 where such ripples are absent. From the detailed analysis in [24] it can be concluded that such ripple-like behavior in Fig. A-4 is due to errors due to fewer number of terms taken in our calculations.
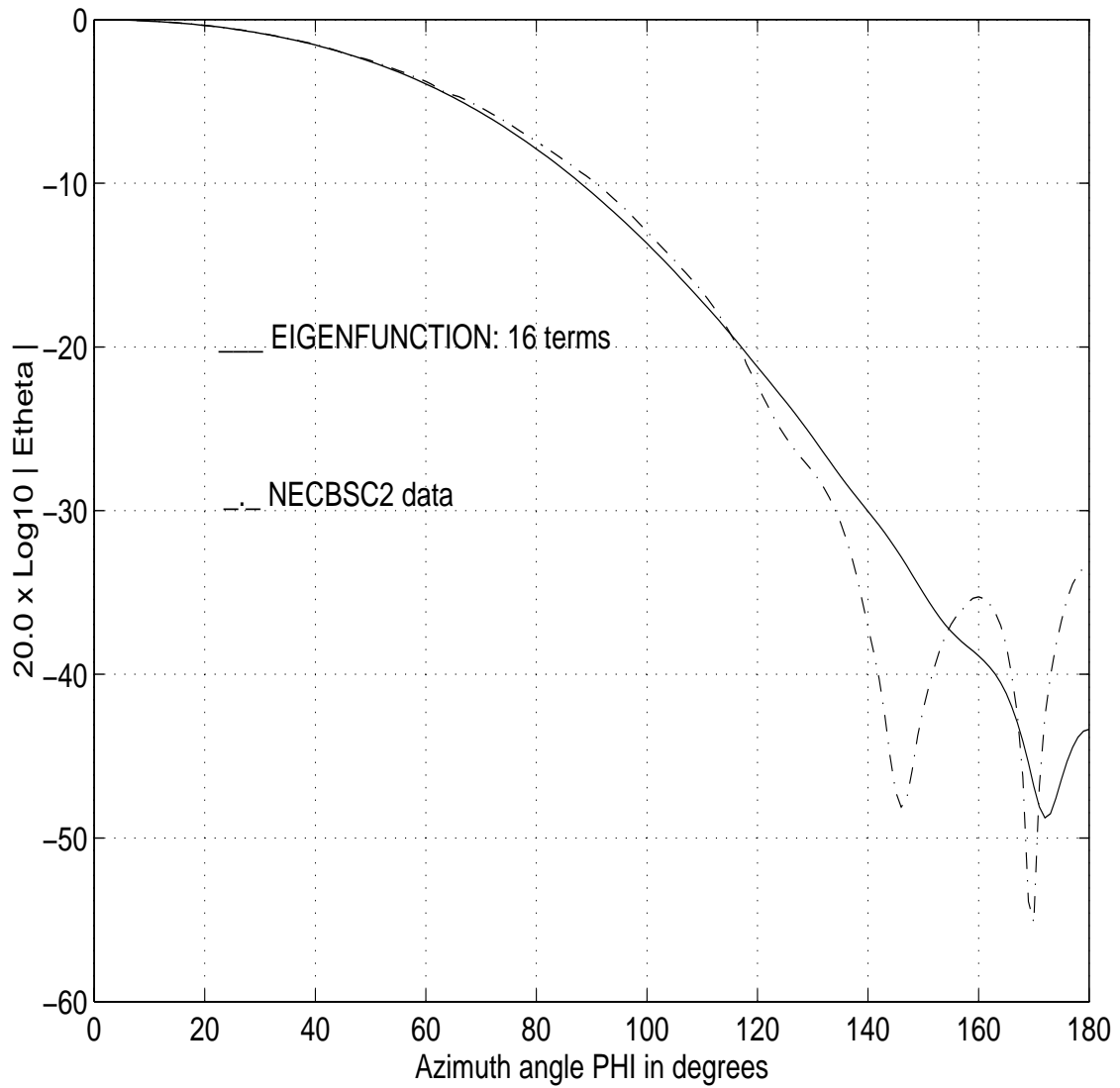
Figure A-1: Eigenfunction and NECBSC2 code comparisons in the $\theta = 90^0$ plane; $ka = 8, k\rho_0 = 8.94, f = 5$ GHz.
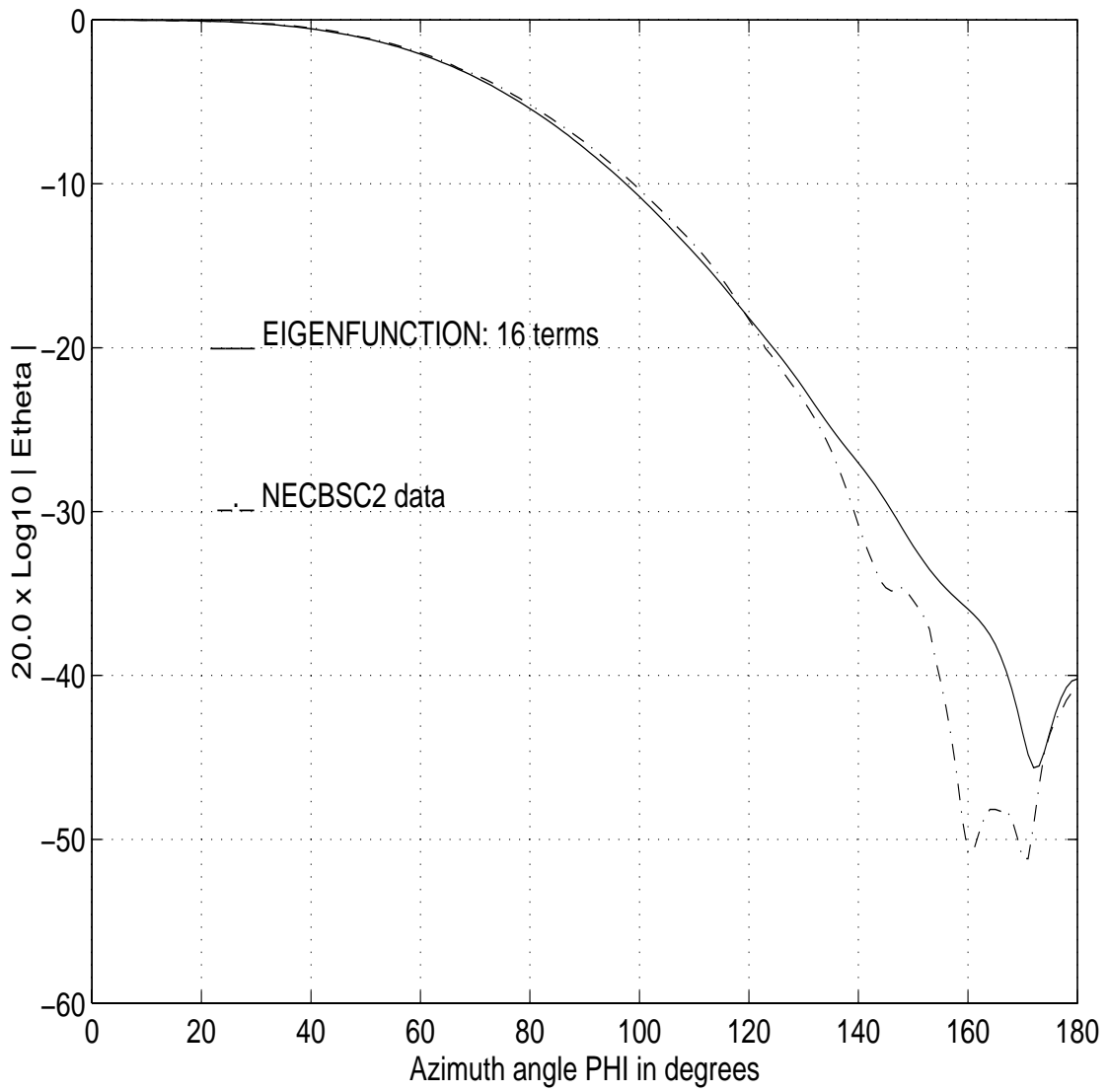
Figure A-2: Eigenfunction and NECBSC2 code comparisons in the $\theta = 90^0$ plane; $ka = 8, k\rho_0 = 9.57, f = 5$ GHz.
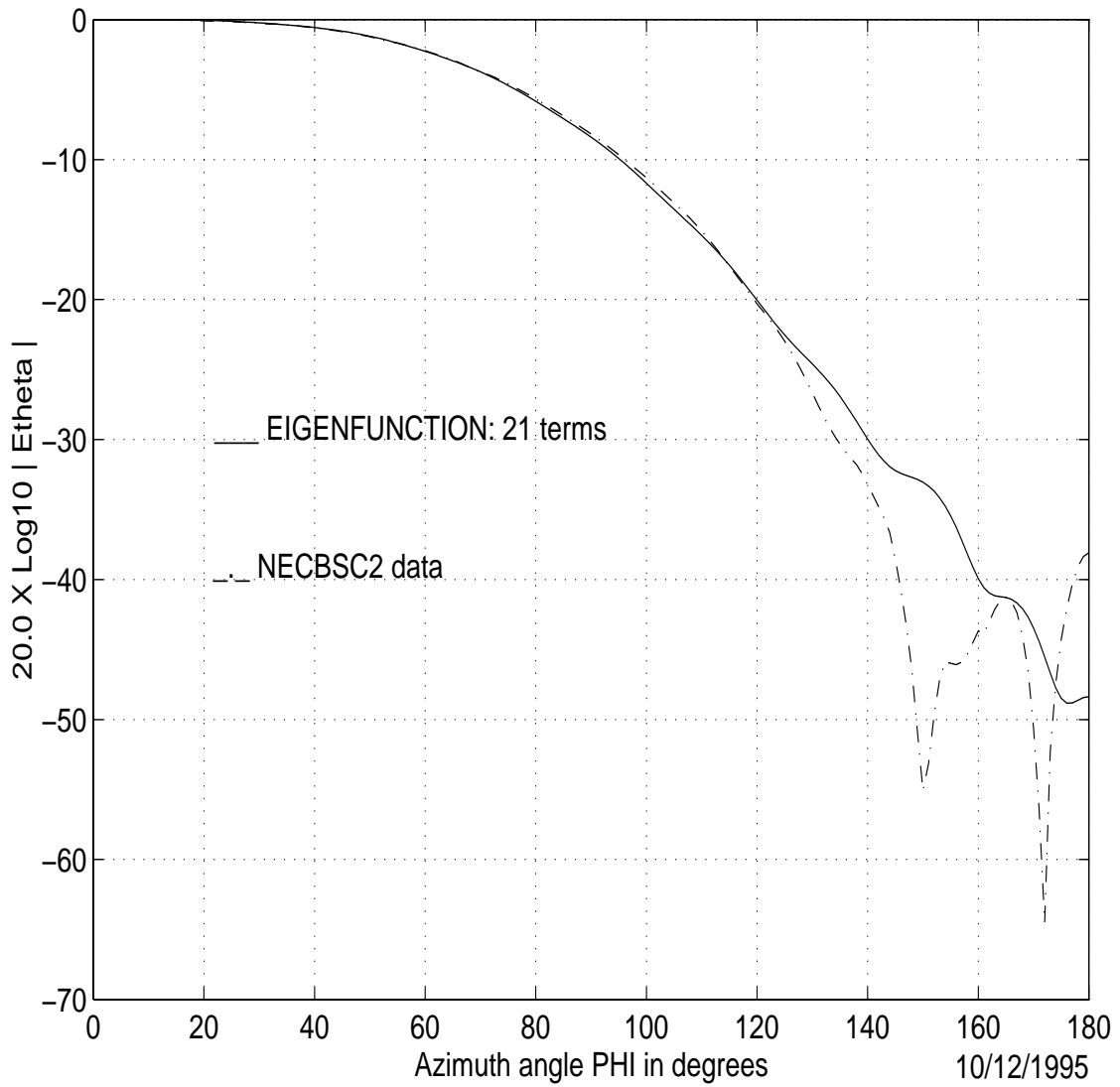
Figure A-3: Eigenfunction and NECBSC2 code comparisons in the $\theta = 90^0$ plane; $ka = 10, k\rho_0 = 11.56, f = 5$ GHz.
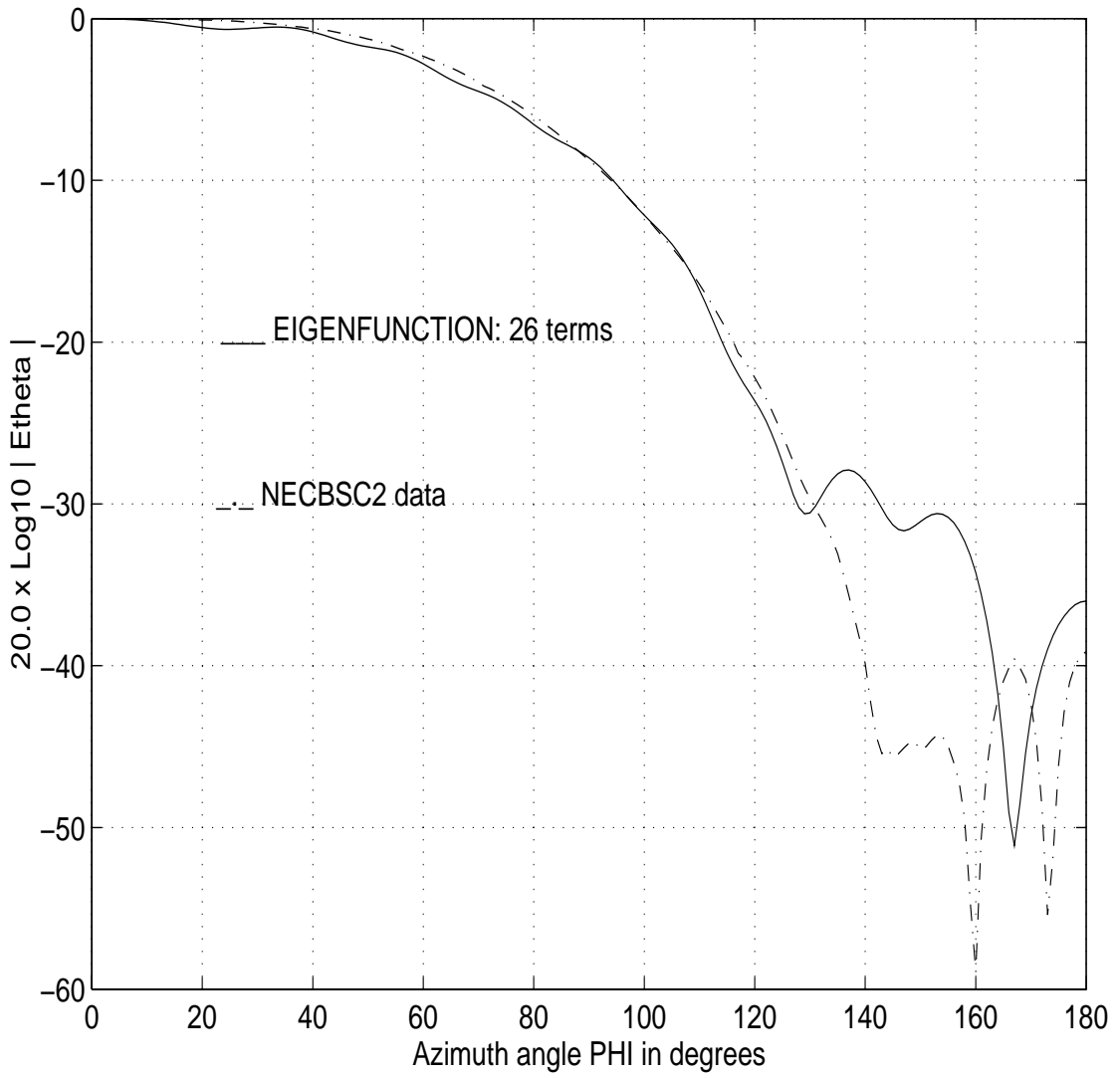
Figure A-4: Eigenfunction and NECBSC2 code comparisons in the $\theta = 90^0$ plane; $ka = 12.5, k\rho_0 = 14.07, f = 5$ GHz.